

PARALLAX OF GALACTIC CEPHEIDS FROM SPATIALLY SCANNING
THE WIDE FIELD CAMERA 3 ON THE HUBBLE SPACE TELESCOPE: THE CASE OF SS CANIS MAJORIS

STEFANO CASERTANO^{1,2,3}, ADAM G. RIESS^{2,1},
JAY ANDERSON¹, RICHARD I. ANDERSON^{2,4}, J. BRADLEY BOWERS², KELSEY I. CLUBB⁵, AVIV R. CUKIERMAN^{2,6},
ALEXEI V. FILIPPENKO⁵, MELISSA L. GRAHAM⁵, JOHN W. MACKENTY¹, CARL MELIS⁷,
BRAD E. TUCKER⁵, AND GAUTAM UPADHYA^{1,8}

(Received; Accepted)
Draft version September 7, 2021

ABSTRACT

We present a high-precision measurement of the parallax for the 12-day Cepheid SS Canis Majoris, obtained via spatial scanning with the Wide Field Camera 3 (WFC3) on the *Hubble Space Telescope* (*HST*). Spatial scanning enables astrometric measurements with a precision of 20–40 μas , an order of magnitude better than pointed observations. SS CMa is the second Cepheid targeted for parallax measurement with *HST*, and is the first of a sample of eighteen long-period ($\gtrsim 10$ days) Cepheids selected in order to improve the calibration of their period-luminosity relation and eventually permit a determination of the Hubble constant H_0 to better than 2%. The parallax of SS CMa is found to be $348 \pm 38 \mu\text{as}$, corresponding to a distance of $2.9 \pm 0.3 \text{ kpc}$. We also present a refinement of the static geometric distortion of WFC3 obtained using spatial scanning observations of calibration fields, with a typical magnitude $\lesssim 0.01$ pixels on scales of 100 pixels.

Subject headings: astrometry: parallaxes—cosmology: distance scale—cosmology: observations—stars: individual: SS CMa—stars: variables: Cepheids—supernovae: general

1. INTRODUCTION

A precise test of the cosmological model can be performed by combining present cosmic microwave background (CMB) measurements (Bennett et al. 2013; Planck Collaboration et al. 2015) with a percent-level determination of the local Hubble constant H_0 (Hu 2005). More than 70 years of work from Hubble (1929) through the first decade of observations with the *Hubble Space Telescope* (*HST*) have resulted in a $\sim 10\%$ measurement of H_0 (Freedman et al. 2001; Sandage et al. 2006), with much of the remaining uncertainty being of a systematic nature. Riess et al. (2011) sharply reduced the uncertainty to 3.3%, to a value of $73.8 \pm 2.4 \text{ km s}^{-1} \text{ Mpc}^{-1}$, thanks to four improvements in the distance ladder consisting of Cepheids and Type Ia supernovae (SNe Ia): (1) calibrating eight modern SNe Ia with Cepheids, (2) observing Cepheids in the near-infrared (NIR) to reduce the impact of extinction and metallicity, (3) the use of two new geometric calibrations of Cepheids—parallaxes of Galactic Cepheids from the *HST* Fine Guidance Sensor (FGS; Benedict et al. 2007) and the 3% geometric maser distance to NGC 4258 (Humphreys et al. 2013, and references therein), and (4) calibrating all extragalactic

Cepheid photometry with a single camera, WFC3, to remove cross-instrument zeropoint errors.

While local determinations of H_0 place it in the range of $70\text{--}75 \text{ km s}^{-1} \text{ Mpc}^{-1}$ (see, e.g., the reviews by Livio & Riess 2013 and Freedman & Madore 2010), the predictions from CMB measurements with a ΛCDM cosmology find a range of $67\text{--}70 \text{ km s}^{-1} \text{ Mpc}^{-1}$ (Bennett et al. 2014; Planck Collaboration et al. 2015), indicating tension between the two sets of determinations. Addison et al. (2015) carries out a comparative reanalysis of *Planck* and *WMAP* data (see also Bennett et al. 2013; Planck Collaboration et al. 2015, and references therein), finding that the *Planck* measurements below $\ell \sim 1000$ are consistent with *WMAP*, while higher multipoles may be inconsistent. The apparent discrepancy between local measurements of H_0 and the values predicted from cosmological results may indicate deviation from the ΛCDM model or new physics (see, e.g., Wyman et al. 2014), although Bennett et al. (2014) find that the evidence for a discrepancy is inconclusive. A resolution on the origin and magnitude of this potential tension is best found in improving the measurements themselves, especially those at low redshift, which have a larger statistical uncertainty.

Starting with Riess et al. (2009) and then in Riess et al. (2011), we are following a program of rebuilding the foundation of the local distance ladder by increasing the range and precision of trigonometric parallax measurements in order to reach long-period ($P > 10$ days) Milky Way Cepheids, nearly all of which are beyond a distance of 2 kpc. In Riess et al. (2014, hereafter Paper 1) we presented a new observational approach to achieve parallax accuracy of $\sim 30 \mu\text{as}$ by spatially scanning the WFC3 camera on *HST*. In principle, this method has the promise of achieving a factor of 10–20 improvement over conventional pointed observations or FGS measurements (Bellini et al. 2011; Benedict et al.

¹ Space Telescope Science Institute, 3700 San Martin Drive, Baltimore, MD 21218, USA

² Department of Physics and Astronomy, Johns Hopkins University, Baltimore, MD 21218, USA

³ email address: stefano@stsci.edu

⁴ Département d’Astronomie, Université de Genève, Ch. des Maillettes 51, CH-1290 Sauverny, Switzerland

⁵ Department of Astronomy, University of California, Berkeley, CA 94720-3411, USA

⁶ Department of Physics, Stanford University, Stanford, CA 94305-4060, USA.

⁷ Center for Astrophysics and Space Sciences, University of California, San Diego, La Jolla, CA 92093-0424, USA

⁸ Department of Physics, University of Chicago, Chicago, IL 60637, USA

2007). This method was demonstrated via five epochs of measurements, spaced every six months, of the field around SY Aurigae, a 10-day Cepheid for which we reported a parallax of $428 \pm 54 \mu\text{as}$ (statistical). While confirming the promise of the method, Paper 1 highlighted several improvements in the experiment design necessary to achieve the desired measurement precision of $30\text{--}40 \mu\text{as}$. Most important of these is the selection of targets with a greater number of reference stars in the field, especially those no more than 5 mag fainter than the target Cepheid. We included those considerations in our approved follow-up programs to obtain parallaxes for 18 Galactic Cepheids. The observations of these 18 Cepheids, stretching over five to nine epochs, are now concluding their fifth epoch. Here we present a detailed analysis of the results for the first of these targets, the 12-day Cepheid SS CMa at an expected distance of ~ 3 kpc. The expected precision of the parallax measurement for the target Cepheids and the reference stars in their fields are shown in Figure 1.

In December 2013, the European Space Agency launched the mission *Gaia* (Prusti 2012), which promises to determine the fundamental astrometric parameters for $\sim 10^9$ stars in the Galaxy with unprecedented precision. Its targets will include hundreds of Galactic Cepheids, including the targets of our *HST* program. End-of-mission results from *Gaia*, expected in 2022, are projected to achieve a parallax precision close to $10 \mu\text{as}$ for its bright targets (see Fig. 1), although special procedures will be needed for targets brighter than $V \approx 12$ mag—including most long-period Cepheids close enough to be effective distance-scale calibrators. Early reports from the mission indicate the existence of significant systematic variations of the basic angle—the separation between the two fields of view 106.5° apart which lies at the heart of *Gaia*'s ability to measure absolute parallaxes—on periods close to the satellite spin period (Mora et al. 2014). We are optimistic that internal calibrations will enable a full correction for these variations and the eventual achievement of the full expected mission precision shown in Figure 1 (see, e.g., Michalik & Lindegren 2015). Nonetheless, the availability of an external calibration of comparable, if slightly coarser, precision may also provide a useful verification of the *Gaia* measurements. Assuming that *Gaia* achieves its stated goals, the calibration of the P – L relation for Galactic Cepheids will likely be better than 1% in distance, and provide the ideal anchor for a measurement of the local value of H_0 with unprecedented precision.

The organization of this paper is as follows. In § 2 we describe the refinements since Paper 1 in the use of spatial scanning data to measure high precision, relative astrometry at a single epoch. We also include a description of the calibration observations we have obtained to improve knowledge of the geometric distortion and other instrumental properties of WFC3/UVIS. Section 3 presents the spectroscopic and photometric data we obtained to characterize the properties of the reference stars. We describe in § 4 refinements in the algorithms used to combine multiple epochs of spatial scan data to measure time-dependent astrometry, and we discuss the parallax measurement thus obtained. In § 5 we show how radial-velocity information can be used to obtain bounds on the effect that binarity can have on parallax measurements. Section 6 briefly discusses the

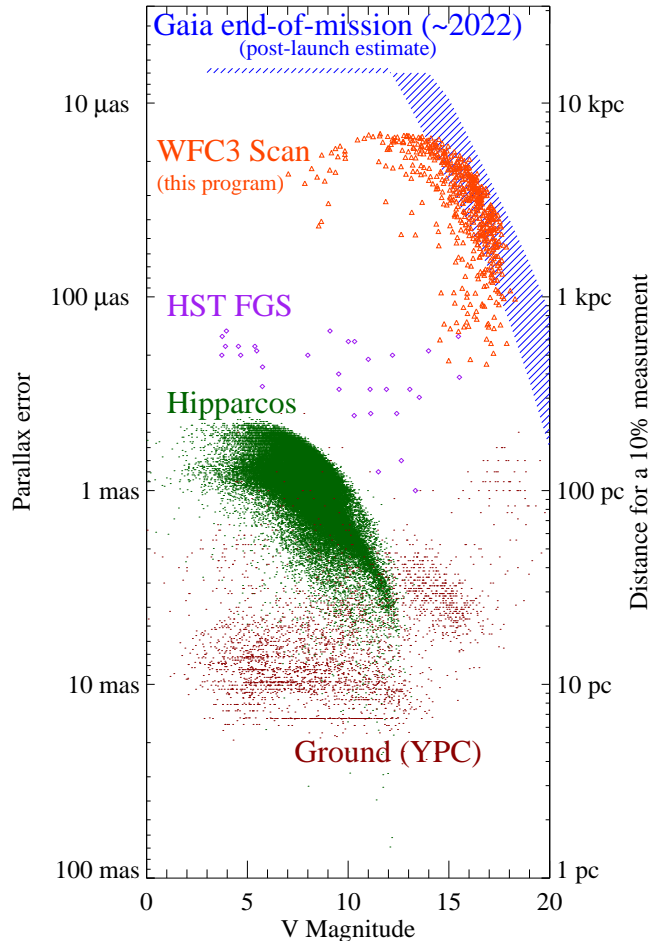


Figure 1. Precision of parallax measurements vs. apparent luminosity from ground and from space, 1995–2022. The right-hand ordinate axis shows the distance at which the error exceeds 10%. (Brown) Ground-based measurements from the Yale Parallax Catalog (van Altena et al. 1995). (Green) stars with a better than $3\text{-}\sigma$ measurement from *Hipparcos* (Perryman 2009). (Purple) Measurements based on *HST*/FGS data (MacConnell et al. 1997; Hershey & Taff 1998; Benedict et al. 2000, 2001, 2002, 2007, 2009, 2011; Nelan & Bond 2013). (Orange) Projected five-epoch precision for target and reference stars from the Cepheid fields observed with *HST*/WFC3 using spatial scanning. (Blue) Range of expected precision for *Gaia* observations, according to the post-launch estimates in de Bruijne et al. (2015). With the exception of a few radio-wavelength measurements (Reid & Honma 2014), only *HST* spatial scanning and *Gaia* can push the 10% precision horizon beyond 1 kpc.

implications of the present and upcoming measurements.

2. MW CEPHEID PARALLAXES: A SAMPLE OF 18 TARGETS.

In Paper 1 we presented our first parallax measurement for a Galactic Cepheid with WFC3 spatial scans, the case of SY Aur. These observations probed for the first time the stability and accuracy of the *HST* focal plane geometry well below the milli-arcsecond (mas) level. Until our scanned observations, the practical limit of relative astrometry with WFC3/UVIS was about 0.01 pixels, or 0.4 mas (Bellini et al. 2011); test data indicated that scanned observations of bright stars over 1000–4000 pixels had the potential to achieve a parallax precision of $20\text{--}40 \mu\text{as}$, about 10 times better than existing measurements. For SY Aur we achieved a final parallax precision of $54 \mu\text{as}$ (statistical). However, we were unable to

fully determine the systematic uncertainty on this measurement, owing to the paucity of reference stars which limited our ability to determine the sensitivity of the result to different processing choices. In many ways, SY Aur was a test case, and the strict requirements of our measurement process were not known at the start of our first 2-year campaign.

On the basis of the analysis of the SY Aur results, we have selected a sample of 18 additional Galactic Cepheids for which we could expect to obtain parallax measurements with uncertainty $\sigma = 30\text{--}40\ \mu\text{as}$ in order to improve the calibration of the Cepheid Period-Luminosity (P - L) relation for the determination of the Hubble constant. Cepheids in this sample are listed in Table 1, with some basic properties; the magnitudes in the Table are as reported by van Leeuwen et al. (2007). Note that our program includes obtaining photometry of the target Cepheids with *HST* in the same filters used for those in SN Ia host galaxies, in order to remove any uncertainties related to differences between ground-based and *HST* photometric systems. The primary considerations in their selection are: (1) period longer than ~ 10 days; (2) ~ 10 reference stars within the field (scan length > 500 pixels) within 5–6 mag of the Cepheid itself; and (3) an estimated distance less than 4 kpc at the $3\text{-}\sigma$ level.

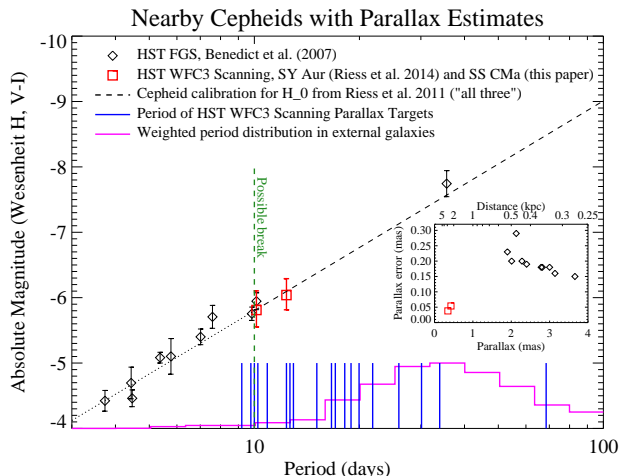


Figure 2. Period-luminosity relation for Galactic Cepheids with trigonometric distance measurement, and period distribution for Cepheids used in the H_0 distance calibration. The open diamonds are the Galactic Cepheids with *HST*-FGS parallax measurements from Benedict et al. (2007), with the Wesenheit absolute magnitude in the H band estimated from their distance and uncertainty. The red squares are SY Aur and SS CMa, with the distances determined in Paper 1 and in this paper, respectively. The dotted/dashed line shows the P - L calibration obtained in Riess et al. (2011) when using all three anchors (Galactic Cepheids, LMC, and NGC 4258). Because of a possible break at $P \approx 10$ days (marked by a vertical green line; Sandage et al. 2004; Ngeow et al. 2009; Kodric et al. 2015, and references therein), the line is shown dotted below 10 days and dashed above. The magenta histogram indicates the distribution of periods for Cepheids in SN Ia hosts (Hoffmann et al. 2016 and Riess et al. 2016, in prep.), scaled to the same total weight for each host. The vertical blue bars show the period of the other Cepheids in our sample (Table 1). Finally, the inset shows the parallax and error for the Benedict et al. (2007) targets (black diamonds) vs. SY Aur and SS CMa (red squares); note that the *absolute* parallax error for SY Aur and SS CMa are much smaller than for the previous targets, but the *fractional* parallax error—and thus the quality of the luminosity calibration—is comparable.

The requirement for a period longer than 10 days stems

from the desire to minimize the impact of systematic uncertainties when using the P - L relation to measure the Hubble constant. Cepheids in external galaxies, especially the hosts of Type Ia supernovae, can be observed with adequate accuracy only if they are sufficiently bright, which implies longer periods. In practice, most of the information comes from Cepheids with periods longer than 10 days. Calibrating the P - L relation with Cepheids of significantly shorter period introduces a systematic uncertainty related to the slope of the relationship. In addition, there are indications that the P - L relation has a break in the neighborhood of 10 days, represented by a change in its slope (see, e.g., Sandage et al. 2004; Ngeow et al. 2009; Kodric et al. 2015, and references therein). If true, this enhances the reason to use as local calibrators primarily longer-period Cepheids, which follow the same P - L relation as the Cepheids in supernova host galaxies. Figure 2 shows the period-luminosity relation for Galactic Cepheids with measured parallaxes, the distribution of periods for the Cepheids in supernova host galaxies (Riess et al. 2016 and Hoffmann et al. 2016, in prep.), and the periods of the Cepheids in our sample.

As shown by our experience with SY Aur, bright reference stars are critical to constrain the relative orientation and variable geometric transformation between scanning mode exposures. Shallow exposures—typically either in narrow-band filters or with the telescope moving faster than $1''\text{ s}^{-1}$ —are needed to observe the $V \approx 9$ mag Cepheid without saturation. Deep exposures in a broadband filter are needed in order to measure enough reference stars ($V < 17$ mag) to provide a well-constrained absolute parallax, as discussed in § 4. Shallow and deep scanning observations are obtained within the same orbit, but the analysis of SY Aur data shows that the geometric distortion varies enough within a single orbit, due to the *HST* day-night cycle, that a second-order polynomial term is needed to account for its change. Unless about 10 or more stars are available to determine the second-order polynomial correction, the uncertainty from the correction dominates the uncertainty in the Cepheid measurement. Therefore we require that at least 10 stars be observable in the shallow exposures with signal-to-noise ratio > 30 per pixel, which implies stars no more than 5 mag fainter than the Cepheid, and scan length of at least 500 pixels.

Finally, the requirement on estimated distance ensures that a nominal error of $\sim 30\ \mu\text{as}$ in parallax translate into a $\sim 10\%$ distance error for each target. Assuming that each Cepheid is at a distance consistent with the current P - L calibration, a final parallax error of $30\ \mu\text{as}$ for each Cepheid, combined with adequate photometry, would result in a collective calibration of the P - L relation to approximately 0.04 mag, or 2% in distance, a significant improvement over the 3% uncertainty of the NGC 4258 calibration (Humphreys et al. 2013).

2.1. *HST* Observations

For each Cepheid, we obtain *HST* observations in five to nine epochs at 6 month intervals, ensuring that the observations are always executed at orientations 180° apart to within the *HST* pointing precision (about 0.01°). The reason is that our measurements are inherently one-dimensional; we obtain very accurate positions perpendicular to the scanning direction, and much less accurate

(often less so than direct observations) in the direction along the scan. In order to optimally measure the *variation* in position of the Cepheid, we need to ensure that the direction of resolution is always nearly the same.

To the extent possible, we also need the scan direction to be fixed with respect to the detector frame, and close to the detector Y direction. This minimizes the impact of low-level geometric distortion, for which only the X component is needed, and of the Charge Transfer Efficiency (CTE) effects that are well-documented with space-based charge-coupled devices (CCDs; see, e.g., Anderson & Bedin 2010). In particular, the CTE losses are much smaller in the detector X direction (Anderson 2014a); consequently, it is desirable for the measurement direction to nearly coincide with the detector X direction. (A small angular offset is introduced in order to vary the pixel phase along the scan.) The motion of the Cepheid in the resolution direction is the result of the combination of the appropriate component of the proper motion and of the parallax of the target, compared to that of the reference stars. Ideally, the date and orientation of each observation should be chosen to maximize the projection of the parallactic motion along the resolution direction. Because of the 180° change requirement, the date and allowed orientation range of each observation are constrained, typically resulting in a projection factor of 0.8–0.9. We allow for a slack of up to one week in the scheduling of each observation.

At each epoch, we obtain four or five scanned observations. The first four are straight scans in the sequence: Forward, deep; Backward, shallow; Forward, shallow; Backward, deep. This sequencing helps average out time variations between deep and shallow scans, which could otherwise lead to larger systematic differences between deep scans (for most reference stars) and shallow scans (for the Cepheid and the brighter reference stars).

If possible, a fifth scan is obtained in so-called “serpentine” mode, in which the scan speed is increased to a value sufficient to avoid saturation of the target Cepheid in the broad-band filter, typically of order of $1''\text{--}4''\text{ s}^{-1}$ (up to an order of magnitude faster than the straight scan). With such a high scan speed, the length of the scan in the standard 350 s exposure time exceeds the size of the detector. Thus, in order to fit the length of the scan, it is necessary to “fold” the scan itself: the telescope describes a series of parallel forward and backward scans, offset by a user-selectable amount in the X direction. We use a separation of $4''$, about 100 pixels. These scans are more complex to analyze and are more affected by potential cross-contamination (overlap between scans pertaining to different stars) because of the higher density of scans, but they offer the potential for direct comparison of the Cepheid and many of the reference stars within the same filter, and they can improve the measurement precision since more pixels are covered. Discussion of the analysis of serpentine scans can be found in § 2.6.1.

As described in Paper 1, in addition to the scanned observations we also obtain short, pointed observations of the field in order to determine multi-band photometry of the reference stars in several medium-band filters, including WFC3’s analogs of the Strömgren filters. The photometry thus obtained, combined with infrared JHK photometry from the Two Micron All-Sky Survey

(2MASS; Skrutskie et al. 2006), space-based photometry at 3.6 and $4.5\ \mu\text{m}$ from the *Wide-field Infrared Survey Explorer* (*WISE*; Wright et al. 2010), and ground-based medium-resolution spectra, is used to obtain spectrophotometric distance estimates of as many of the reference stars as possible, which is a critical step in converting the relative parallax measurement for the Cepheid target into an absolute measurement. Details on the spectrophotometric data and distance estimates are in § 3; the estimate of absolute parallax is discussed in § 4.

2.2. The Case of SS CMa

Here we present the results of the analysis for the first of these 18 targets, the fundamental-mode Cepheid SS Canis Majoris (SS CMa), with a period of 12.35 days and a mean magnitude $\langle V \rangle = 9.9$ mag. SS CMa was identified as variable by Hoffmeister (1929), and a period was determined by Oosterhoff (1935). We have chosen to complete the analysis of SS CMa because it is one of the first few Cepheids for which five epochs of observations have been completed, and because we believe that it is representative of the possible accuracy of the parallax measurements for the rest of the targets of our program.

Figure 3 shows a mosaic of the region of sky around SS CMa in the filter F547M, as obtained from the very short observations included in our program. The area represents approximately 2 WFC3/UVIS fields of view, stacked vertically with an overlap of $\sim 20''$. Reference stars and their designations are indicated. The Cepheid (Star 0) is saturated. The diagonal bands are caused by the gap between the two detectors in WFC3/UVIS; more observations in the future will help cover this gap. Figure 4 shows a normal scan (top) and a serpentine scan (bottom); serpentine scans are discussed further in §§ 2.4 and 2.6.1.

The Cepheid SS CMa has been discussed in the literature as a potential binary. Evans & Udalski (1994) identify a nearby faint blue star (Star 29 in Fig. 3; $13''$ from the Cepheid, $V \approx 15.51\text{--}15.58$ mag) which they argue is likely to be a physical companion, on the basis of its estimated distance modulus and of probabilistic arguments. We will show in § 4 that astrometric and spectrophotometric evidence suggests that Star 29 is significantly closer than the Cepheid, and therefore not a physical companion. Szabados (1996) reports an apparent difference of $\sim 15\ \text{km s}^{-1}$ between the radial velocities (RVs) measured by Joy (1937) and Coulson & Caldwell (1985). If interpreted as caused by binarity, this measurement would indicate a massive companion in an orbit with period from a few up to 20 years, depending on its eccentricity.

Binarity can potentially bias the astrometric parallax determination if the orbital motion of the Cepheid itself, sampled at the times of the astrometric observations, has a sufficient component to contribute to the parallax signature. This is most likely for orbits with period ~ 1 year; very long-period binaries will produce primarily a proper-motion bias, and short-period binaries have a small astrometric signature that will typically average out in the measurements.

For the case of SS CMa, we have obtained new RV measurements, discussed in detail in § 5, which demonstrate that the contribution of binary motion compatible with the observations is most likely below a few μas , thus

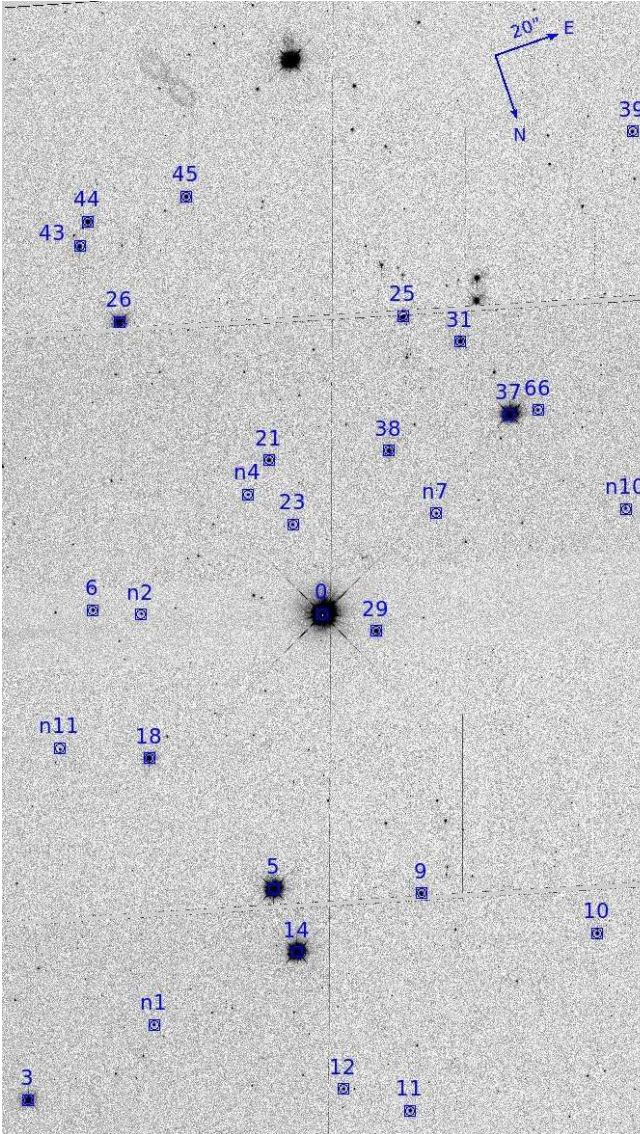


Figure 3. Mosaic of direct *HST* image of the field around S CMa in filter *F567M*, obtained with WFC3/UVIS in 2×2 binne mode. The Cepheid at the center of the field is saturated. The image results from a mosaic of two exposures vertically displaced by $\sim 20''$ in order to cover the full field appearing in the scanned images. The two diagonal gaps result from the separation between the WFC3/UVIS detectors. Reference stars used in the analysis are marked with the identification reported in Table 2. Star 29 is the putative companion of SS CMa.

significantly smaller than the uncertainty in the parallax measurement.

2.3. *HST* Spatial Scans for Astrometry

In Paper 1, we demonstrated that for sufficiently bright sources, scanning-mode *HST* observations, in which the telescope is slewed during the exposure and each star leaves a trail of light nearly along a pixel axis, can achieve positional measurements with a precision up to 0.5-1 millipixels (1 millipixel, or mpix, is about $40 \mu\text{as}$) in the direction perpendicular to the scan, about a factor of 10 better than optimal measurements from pointed images. However, we also discovered that at the millipixel level, several systematic effects come into play and need to be properly calibrated in order to fully realize a correspond-

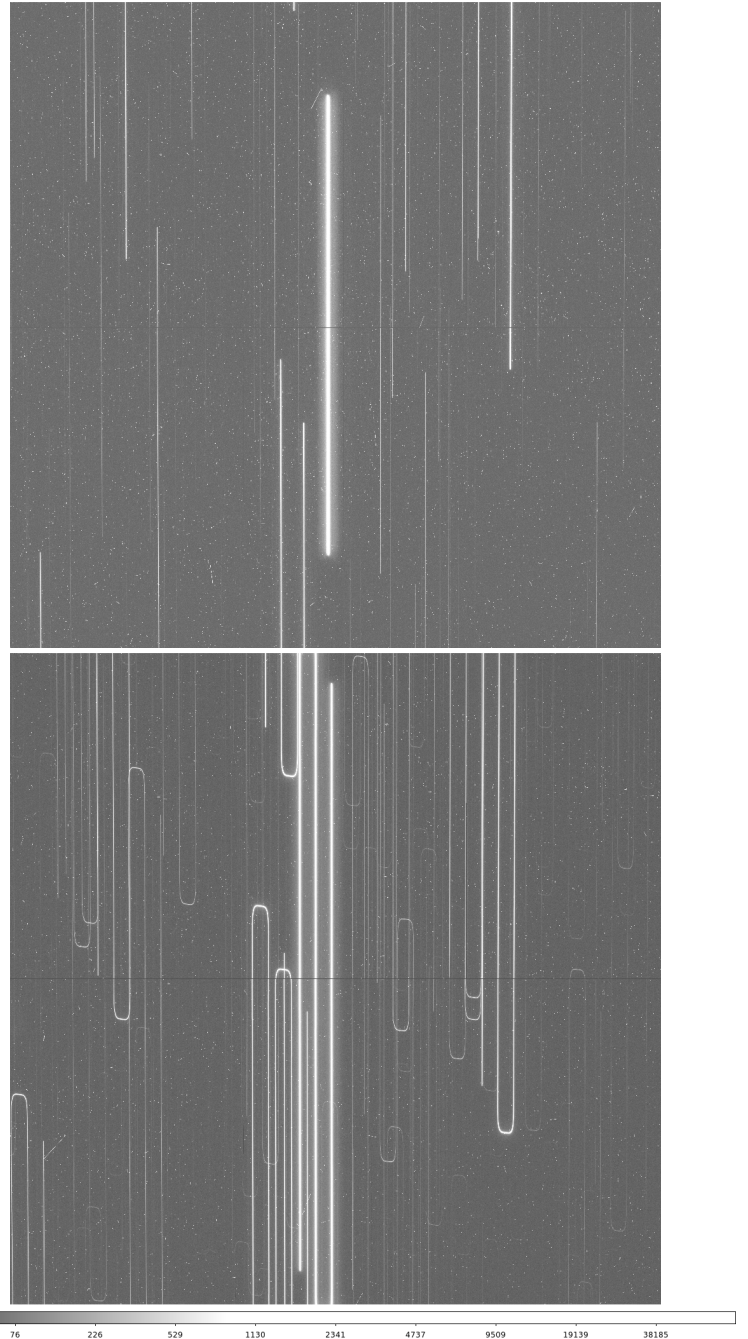


Figure 4. (Top) Direct scan of the SS CMa field in *F621M*. The central strip is the Cepheid, which is not saturated in this image. (Bottom) The serpentine scan obtained in *F606W*. For this image, the scan speed of the telescope was sufficiently high that the Cepheid does not saturate, resulting in a total scan length of over 8000 pixels. Consequently, the scan is folded twice, resulting in three separate legs for each star.

ing accuracy of $\lesssim 40 \mu\text{as}$ in the parallax measurement.

Perhaps the most problematic systematic effect is in the insufficiently characterized, and variable, geometric distortion solution for the WFC3/UVIS camera. The mapping between pixels and the sky is well established and calibrated for direct images, with a residual uncertainty currently estimated below 0.6% of a pixel (root-mean square) over the field (Bellini et al. 2011)—fully adequate for the astrometric interpretation of direct, pointed images. However, this uncertainty is an order of

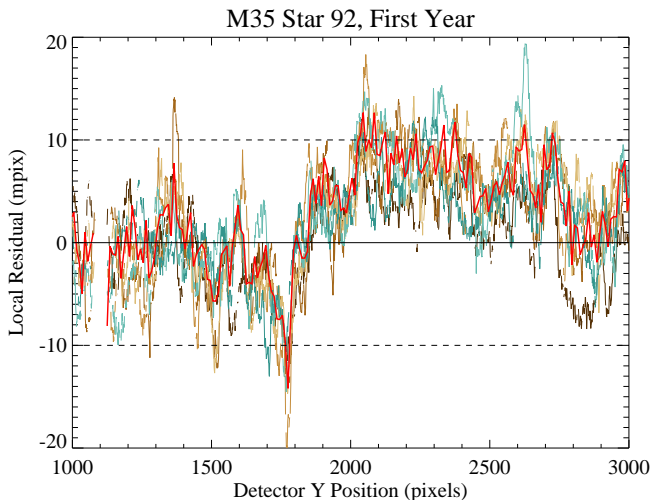


Figure 5. Repeatability of the differential geometric distortion over a 2-orbit time period. The thin colored lines show the offset in the detector X direction for a single bright star in M35 over repeated scans, smoothed over 20 pixels, and expressed in millipixels. The horizontal dashed lines indicate the nominal precision of the standard geometric distortion, 0.01 pixels. The thicker red line is the mean differential distortion and has a root-mean square (RMS) amplitude of 6.0 mpix; the RMS difference between individual lines and the mean is 4.0 mpix. The typical statistical measurement uncertainty for this star is ≈ 2 mpix per smoothed pixel per scan, and under 1 mpix per cell.

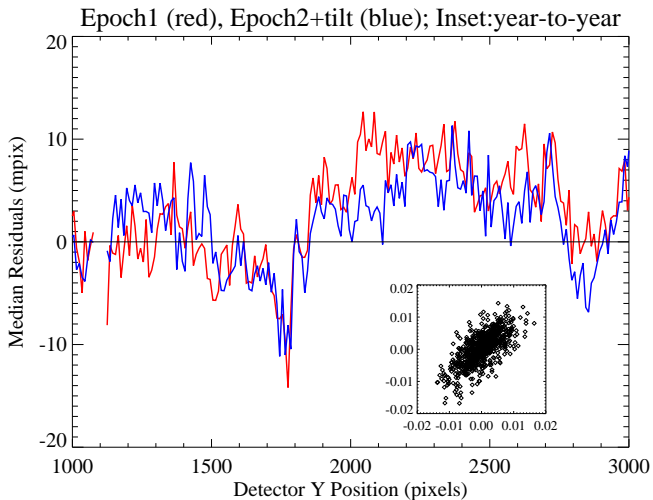


Figure 6. Comparison between the differential geometric distortion measured for the same star in the same detector location one year apart. The red line is the same as in Figure 5; the blue line is the result of the same measurement a year later, with a global tilt removed. The measurements track one another very closely, demonstrating that the local differential geometric distortion remains constant over a one-year period. The RMS difference between the lines is 3.9 mpix, corresponding to a repeatability of about 2.8 mpix. The inset shows the differential distortion measured in each 100×100 pixel cell in Year 1 (abscissa) vs. Year 2 (ordinate), expressed in pixels. The year-over-year correlation coefficient is 0.70.

magnitude higher than the requirements of our program. Calibration observations of the field of M35, obtained one year apart in 2012 and 2013, show that much of the residual geometric distortion at the sub-0.01 pixel level is static and smooth, in that the residuals vary slowly over the field of view (on scales of ~ 100 pixels) and are highly correlated from year to year.

Figure 5 shows that the pattern of residual geometric distortion is repeatable over short (orbital) time scales. Each line shows the variation in the measured X position along the scan for the same bright star, located at the same detector position, in several consecutive scans over a two-orbit period, after subtracting the jitter pattern for that observation. To reduce pixel-to-pixel noise, the lines have been smoothed with a 20-pixel length. Without residuals in the geometric distortion or other disturbance factors, these lines should all be consistent with zero (i.e., a constant X position along the scan). Instead, there is a definite pattern of deviations, and this pattern is consistent from scan to scan. The horizontal dashed lines indicate the nominal precision of 10 mpix for pointed observations, which is also the expected accuracy of the standard geometric distortion solution. This distortion pattern repeats closely even a year later: Figure 6 shows the median pattern for the same star in the same sets of observations taken one year apart. (Consistent with our treatment of all scans, an overall tilt of the lines has been solved for and subtracted.) Again, the patterns are very similar, strongly suggesting that the residual geometric distortion is stable over time. The inset in Figure 6 shows the measured differential geometric distortion in each cell in Year 1 (abscissa) vs. Year 2 (ordinate); the two quantities are highly correlated ($r \approx 0.70$), showing that a significant part of the distortion remains the same from year to year over the whole field of view.

However, the differences between scans in the same year, or between years, is larger than nominal statistical errors, which are below 1 mpix per cell. Time-dependent geometric distortion, identified and discussed in Paper 1 for both calibration and SY Aur observations, contribute to these differences. We thus attempt to characterize and correct for both a *static* and a *time-dependent* component of the geometric distortion correction, in different ways.

2.3.1. Static Correction to the Geometric Distortion Solution

Even neglecting the time dependence of the geometric distortion solution, any residual static term will affect our solution. The reason is that parallax observations need to take place approximately at 6-month intervals, and orbital geometry mandates that observations 6 months apart cannot be taken at the same orientation, although they can generally be taken at orientations 180° apart. Thus, for a typical target, there will be three epochs taken at one orientation, and two taken at an orientation different by 180° . Changing the telescope roll by 180° ensures that the resolution direction, perpendicular to the scan direction and thus typically along the detector X direction, remains the same on the sky, thus greatly simplifying the analysis and improving the accuracy of the results.

Target and reference stars can be placed essentially at the same detector location for each orientation; as we are interested in *relative variations* in the stars' position, small errors in the geometric distortion solution, which typically behave smoothly over the detector, will cancel out. However, this is not the case across orientations, when each target's location moves to a completely different place in the detector, and thus the accuracy in the geometric distortion solution comes in fully.

In order to improve the static geometric distortion so-

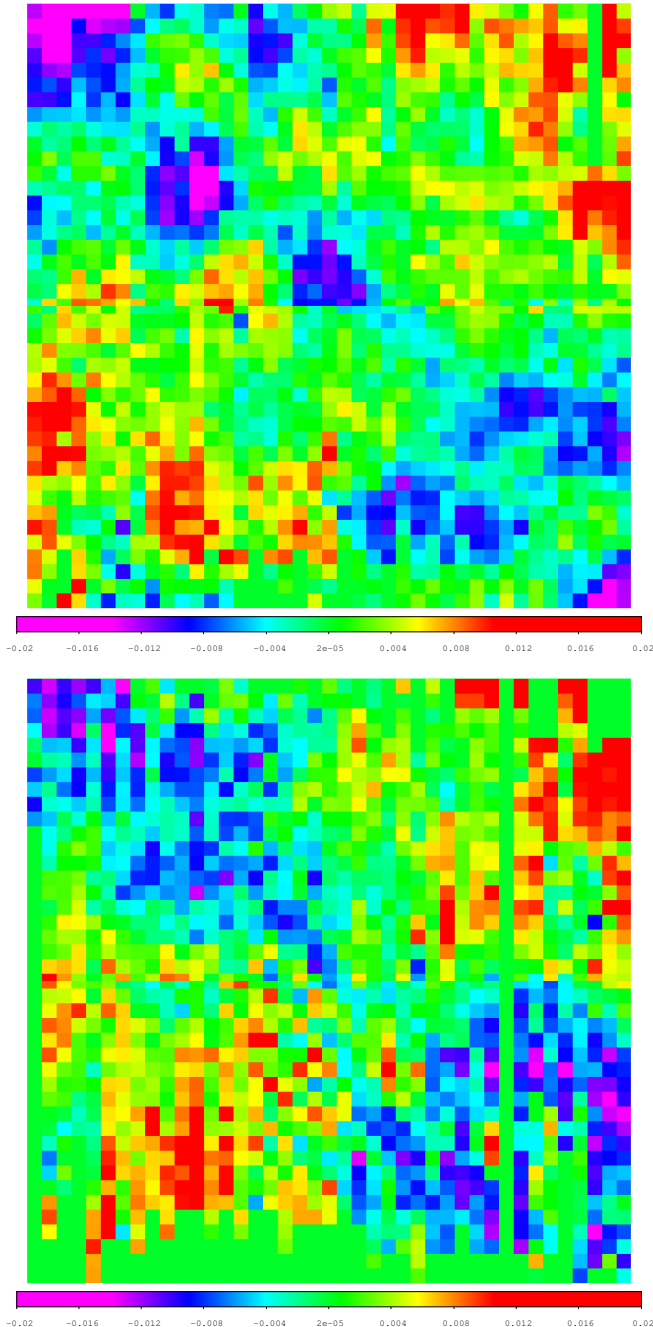


Figure 7. (Top) Pseudo-color representation of the static correction to the default geometric solution in the X direction for $F606W$, averaged over 100×100 pixel cells. The correction was obtained from scanned observations of a field in the open cluster M67. A total of 20 X dithers were obtained in order to cover the detector as well as possible. The color bar ranges from -0.02 to 0.02 pixels. Over most of the field of view, the correction is less than 0.01 pixels (blue to orange), but there are small regions with large corrections (negative: purple, positive: red). (Bottom) Same for $F621M$, from 15 dithers in the open cluster M48 to better match the sensitivity of the narrower filter. The overall pattern is similar to $F606W$ (see also Fig. 8). About 5% of the cells have no measurement.

lution, we have analyzed calibration observations taken of two open clusters, M48 and M67, which offer a wealth of bright stars and thus allow a dense sampling of the detector in as few as 10 dithers. Such observations have been obtained as part of the Cycle 22 WFC3 calibration program, and have demonstrated that a static term,

sampled on a grid of 100×100 pixel cells, can account for about half of the deviation from an accurate solution. (The differences remain larger than the statistical measurement errors, which are below 1 mpix, in part because of the time-dependent correction discussed in Section 2.3.2.) We therefore employ this solution as a correction to the default geometric distortion solution obtained by Bellini et al. (2011). The pattern of static geometric distortion thus obtained is shown in Figure 7; the top panel is for $F606W$, and the bottom panel for $F621M$. The two patterns look remarkably similar; Figure 8 shows the strong correlation ($r \approx 0.7$) between the geometric distortion corrections thus obtained, despite the fact that the observations targeted different star fields, in different filters, and were taken more than a month apart.

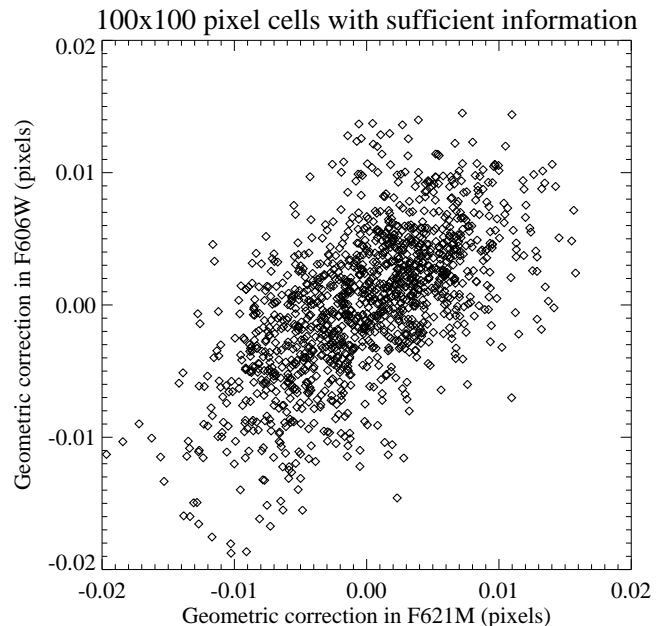


Figure 8. Comparison between the geometric distortion residuals in $F621M$ and $F606W$, respectively, for each 100×100 pixel cell in the detector. There is a clear correlation between the residuals, indicating that the bulk of the correction is in common between filters. However, about 30% of the residual correction, as determined from these measurements, differs between the filters, suggesting that a better correction is achieved with a filter-specific correction.

2.3.2. Time-Dependent Correction

Even for observations obtained with stars at exactly the same location and in back-to-back exposures, we find that there is a smooth variation in the relative positions measured for each star, which generally can be well approximated as a low-order polynomial function of the position on the detector. This variation appears correlated with the nominal focus position of the telescope, which is provided after the fact by the Space Telescope Science Institute (STScI) Telescopes group as a result of a temperature-based model of the telescope’s optical train (<http://www.stsci.edu/hst/observatory/focus/FocusModel1>). There is also a suggestion that the polynomial coefficients are correlated, and in fact a principal-component analysis (PCA) of the correction polynomial shows that

two or three parameters suffice to account for over 95% of the correction.

Although the correlations of the polynomial correction with focus and internally across coefficients are highly indicative, we do not yet have sufficient information to characterize the required correction directly from estimated focus. We therefore resort to a self-calibration approach, in which the polynomial distortion is part of the model and is chosen so as to minimize the source-by-source residuals of the full set of observations across epochs.

2.4. Designing the Observations

Based on our experience observing the field of SY Aur (Paper 1), we developed simulation tools to optimize the observations of other Cepheids and we applied these to the field of SS CMa. As in SY Aur, we selected positions, scan speeds, scan lengths, and filters to allow the highest quality parallax measurements from the field (see Paper 1 for these details). The field of SS CMa provided more than twice as many reference stars of intermediate brightness, used to register the deep and shallow scans, as the field of SY Aur.

In addition to the straight scans we discussed in Paper 1—two each in broad and narrow-band filters at each epoch—we have also obtained and processed *serpentine* scans, in which the telescope moves through the field in a boustrophedonic pattern (down to up, shift right, up to down, shift right, etc.), as shown in the bottom panel of Figure 4. With this pattern scanned at a rate of $1.5'' \text{ s}^{-1}$, the target Cepheid does not saturate even in the broad-band filter. However, at this rate the telescope will traverse about $525''$ over a 350 s exposure, almost four times the WFC3 field of view. Taking exposures shorter than 350 s is not desirable because of how memory is managed in WFC3; therefore, in order to keep the target and most of the reference stars on chip for the largest fraction of the time, and thus to collect as many photons as possible, the scan pattern is folded into multiple near-straight scan lines, all approximately along the Y direction, with small “crossbars” between them. In the case of SS CMa, the $F606W$ serpentine scans had three legs, and the overall length was such that no crossbars are visible for the Cepheid; the turnaround occurred while the Cepheid was off-chip. Owing to planning priorities, no serpentine scan was obtained in the fifth and final epoch.

The advantage of the serpentine scanning pattern is that the Cepheid and most of the reference stars are observable in the same exposure; thus, it is possible to solve directly for relative and absolute parallaxes without the potential for inconsistencies in the geometric distortion solution across filters. The disadvantages are that (1) the telescope scans faster than in the narrow-band frame with equivalent count rate, therefore providing less local contrast against the sky background for faint reference stars (this is partially compensated by the larger number of points per star); (2) the exposures are more crowded, with a greater chance that otherwise fine reference stars will be marred by an overlapping trace from a different star, and (3) the motion of the telescope is more complex, and it is more difficult to identify fixed points such as the start and end of each scan. For example, for SS CMa the scan length in the middle leg exceeds the size of the WFC3 instantaneous field of view, so that neither its

start nor its end are visible. Thus, it is more challenging to determine the position of the reference points along each leg, other than the overall start and end. These difficulties notwithstanding, we have been able to process serpentine scans with methods similar to our other scans, and the results are incorporated in our astrometric solution (see § 2.6.1).

2.5. Analysis of Scan Data

The analysis of the scan data for SS CMa largely follows the pattern we described in Paper 1 for SY Aur. The key steps are: (1) identifying the pixels associated to each trail (star); (2) defining a minirow-by-minirow detector X position at each location along the trail by a one-dimensional fit of the observed signal along each minirow with a spatially variable line-spread function (LSF); (3) converting the position into rectified coordinates using the distortion map; (4) removing the effects of jitter and variable rotation; (5) determining the relative rectified X position for each star in each image; (6) combining the measurements from multiple scans within each epoch, including both deep and shallow frames; and, finally, (7) estimating the parallax of each target on the basis of the combined astrometric and spectrophotometric information. Key differences in the processing for SS CMa are: (1) the availability of an improved geometric distortion solution via the static correction discussed in § 2.3.1; (2) the use of serpentine scans, which are combined with deep and shallow frames for each epoch; and (3) the introduction of an empirical correction for the X -direction CTE loss (X-CTE). Thanks to the number and quality of reference stars, the nominal error of the parallax for SS CMa is significantly smaller than for SY Aur. We will now discuss in detail each step, highlighting the changes with respect to Paper 1.

Our astrometric measurements are based on the spatial scan exposures listed in Table 3; Figure 4 shows typical examples of straight and serpentine scans.

The nearly vertical “trails” are the images that each star leaves as the telescope scans over the field. The length of the straight scans is $\approx 144''$, 88% of the length of the field of view of WFC3/UVIS; thus, the part of the sky covered during the scan is almost twice the normal field of view of the camera. Stars near the center of the region spanned in the detector Y direction will have trails that start and end within the frame, while stars farther from the center along Y have trails that enter or leave the frame during the scan. For serpentine scans, the telescope motion is more complex; the vertical portions are scanned at $1.4'' \text{ s}^{-1}$, about 35 pixel s^{-1} , a speed chosen to avoid saturation of SS CMa in filter $F606W$. However, at that scan speed, and given the desired exposure time of 350 s, the total length of the scan is $\approx 525''$, over three times the field of view of the detector. Therefore the scan is folded, consisting of three vertical legs separated by $4''$ in the detector X direction. The turnarounds for the Cepheid occur just outside the detector field of view; other stars, at lower (higher) Y position, can have their first (second) turnaround within the field of view.

Note that all celestial sources in the field are extended because of the motion of the telescope. Cosmic rays are the only compact sources in the frame and are readily identified by their lack of spatial extent, allowing us to identify and disregard impacted pixels.

We used a master catalogue of stars to first simulate and then match the observed trails to these stars. The fidelity of the simulations is a few pixels, and in many cases minor adjustments are needed to ensure that the full 15-pixel window around each trail pixel is fitted. We also use the simulations to identify the regions within each star’s trail that are affected by nearby star trails, and disregard the impacted pixels if the simulation indicates a bias of greater than 1.5 mpix for a given row.

The case of serpentine scans is more complex. For serpentine scans, each star’s trail is marked by multiple reference points: the overall start and end, which are the start of the first leg and the end of the last leg, and whose location is determined by the shutter opening and closing; and the turnarounds between legs, whose location is determined by the motion of the telescope. For any given star, only a subset of these points is visible in the image. Furthermore, we have found that the relative location of these reference points cannot be predicted with sufficient precision from image to image, and therefore it has to be determined empirically from the data themselves. Locating individual trails in a serpentine image is thus a two-step process: first, locate the start, end, and turnaround points for a subset of well-exposed stars at various locations in the field of view; second, determine the geometry of the scan (with an accuracy of ~ 3 pixels) and apply this geometry to predict the serpentine trails of all the stars visible in the scan using our star catalogue. The latter include stars too faint to be profitably measured, but that are still bright enough to “spoil” the scans of brighter stars, as described above. The trail map must then be inspected and reference points tweaked to improve the match with the data; at the end of this labor-intensive process, we were generally able to identify and locate the trails of individual stars to within ~ 1 pixel.

For the purpose of subsequent analysis, trails in serpentine scans are split into individual passes, each including the trails of all relevant stars in that pass. This allows us to associate together photons collected at the same time, and consistently solve for time-dependent effects, such as the variable field rotation discussed below. It also allows for a more careful identification of spoilers, since different legs can have different spoiler impact. In the case of SS CMa, each 3-leg serpentine scan results in three separate position measurements for all the stars, thereby associating together measurements taken at the same time. Note that the serpentine scan was *not* obtained during the fifth epoch; thus, Epochs 1 through 4 each have 7 sets of measured positions (5 for the Cepheid), while Epoch 5 has 4 sets of positions (2 for the Cepheid).

As in Paper 1, we independently fit each 15-pixel minirow along the trail to determine the X position of the star at that value of Y . The fit uses an empirical LSF appropriate to the filter and detector position, obtained by integrating the empirical point-spread functions (PSFs) from Bellini et al. (2011) and, like the latter, oversampled by a factor 4. Data quality flags from the detector characterization as well as flags from source-contaminated pixels are used to avoid fitting bad pixels. The end result is an array of detector X positions and uncertainties as a function of the Y -axis position (equivalent to time) along the scan.

Also following the same procedure as in Paper 1, we start with the geometric distortion solution for *F606W*

from Bellini et al. (2011), which uses a definition of the PSF position that is consistent with the empirical determination of the PSF itself. This geometric distortion map is used to transform the detector X and Y positions to sky coordinates. We obtain a similar solution for *F621M* from calibration observations of ω Cen. In addition, in this paper we also correct for the residual geometric distortion obtained from calibration observations of M67 and M48 (§ 2.2.1). The original solution from Bellini et al. (2011) is expected to have an accuracy of ~ 0.01 pixel on scales of ~ 40 pixels; this accuracy is sufficient to reach position precision of 1 mpix ($40 \mu\text{as}$) for full-length scans, which would be a significant contribution to our overall error budget. By applying our new correction, we expect that the local residuals will be reduced to ~ 3 mpix on a scale of 100 pixels, with a projected contribution to the final error budget of $\sim 20 \mu\text{as}$. Again as in Paper 1, we use the time-dependent velocity aberration values provided by the STScI pipeline, interpolated to account for its variation *during* the observation, to correct for the corresponding plate-scale changes along the scans. Later, we account for perturbations in the geometric distortion of the field caused by the day-night thermal cycle of *HST* when registering different scans.

As for the analysis of SY Aur, we define the one-dimensional position measurements for each scan line relative to the mean line of the sample. This mean line or reference line is determined by aligning all scan lines in time and taking their weighted average. The reference line thus contains the jitter history in the direction perpendicular to the scan which is removed from all lines in their difference with the reference. Figure 9 shows the comparison of two bright star trails aligned in scan time and the residuals after subtraction of one from the other. We use the requirement that scan lines, relative to the reference, are parallel on the sky to measure the time dependence of the scan roll angle. The variable rotation history of the scans can be measured well for the two deep scans obtained at each epoch in *F606W*; Figure 10 shows that the rotation angle is very similar in both scans obtained at the same epoch. The variable rotation cannot be measured as accurately in the shallow scans, because of the lower signal-to-noise ratio for all stars except for the Cepheid, which by itself cannot constrain the rotation angle. As the variable rotation term appears to be constant within each epoch, we determine the correction by averaging the measured rotation in the two deep scans at each epoch, and apply the resulting correction to all deep and shallow scans for that epoch. Figure 10 also shows that the variable rotation is markedly smaller in Epochs 3 through 5, most likely because of the improved FGS geometric solution adopted on July 22, 2013, between our Epochs 2 and 3 (Nelan and Lallo, private communication).

2.6. Using Multiple Observations at the Same Epoch

The fundamental measurements at each epoch of observation consist of the relative X position of all stars, obtained from the combination of all coeval scans, deep, shallow, and (if available) serpentine. In order to combine these scans, they must be astrometrically registered, which requires correcting for any differential geometric distortion. As in Paper 1, we include in the distortion

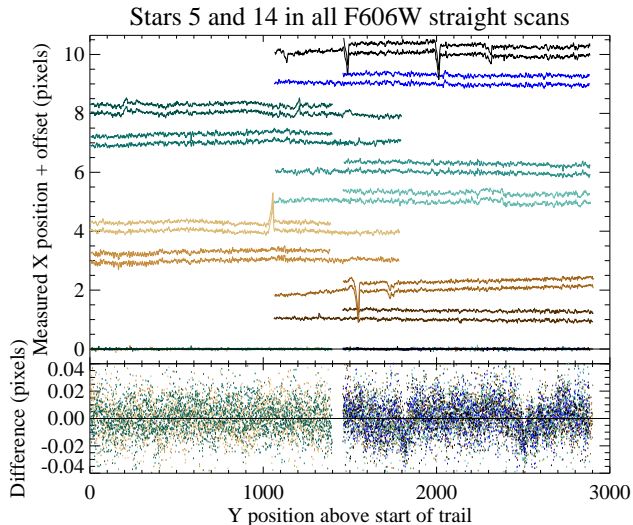


Figure 9. Variations in the measured X position for two bright stars (Stars 5 and 14) in the field of SS CMa in each of the 10 full-length straight $F606W$ scanned exposures. The top panel shows the individual X measurements, with a different color for each exposure. Scans have been offset along the abscissa to match photons received at the same time, and along the ordinate by an arbitrary constant. The very high correlation between the irregularities in the two scans shows that most of the apparent “noise” in the measured position is actually telescope jitter. The differences between the two stars in each exposure are overplotted at $X \approx 0$, and again in the bottom panel with a scale expanded by a factor of 50. The pixel-to-pixel variation in the difference is consistent with the expected uncertainty in the fit for each minirow; the nominal error in the mean separation in each exposure is 0.4 mpix, or 16 μas .

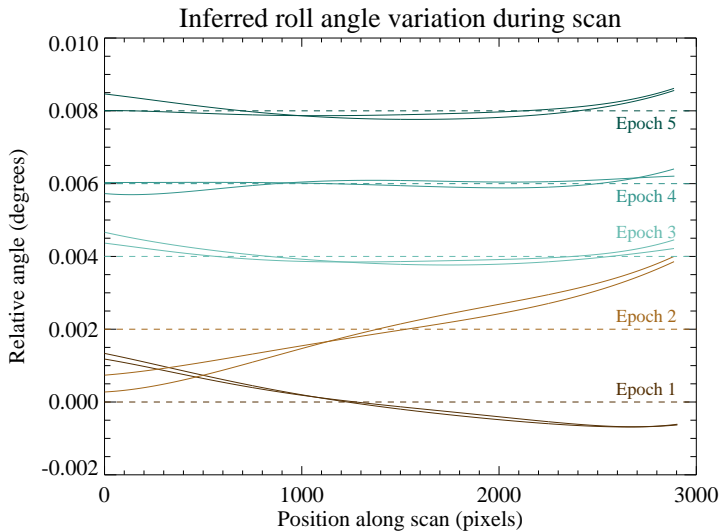


Figure 10. Differential field rotation during the $F606W$ scans in each of the five epochs of the SS CMa observations, represented as a fifth-degree polynomial as a function of position along the scan. A correction for the differential field rotation is applied to the measured X positions along each scan. Note the similarity of the pattern for the two observations obtained at each epoch, as well as the marked decrease in the change starting in Epoch 3, after an improved FGS distortion solution was adopted in July 2013.

model a low-order polynomial correction with free coefficients for each observation after the first. We adopt a polynomial correction to the X coordinate when aligning two frames which depends on the pixel position of each star trail in the detector; the assumption is that

any variation in the transformation from true to measured position is tied to the telescope and detector, and therefore is best described in measured rather than true coordinates. Note that a generic first-degree polynomial includes by definition an X scale term (the first-order correction in X) as well as a *detector* rotation, which is slightly different but closely related to the *field* rotation previously considered. As for M35 and SY Aur, we find that a second-degree polynomial as a function of X and Y coordinates is adequate to describe the X coordinate transformation between two scans. (Only terms of *total* degree up to the polynomial degree are included, so our second-degree polynomial contains terms in $X \times Y$, but not in $X^2 \times Y$ or $X \times Y^2$.) A second-degree polynomial in X and Y has five coefficients (plus a constant term), two of which describe an offset and a rotation, respectively.

For SY Aur we found that a dearth of intermediate-brightness stars, combined with the need to allow for second-order polynomial corrections between the frames, led to significant uncertainties in the transformation of the Cepheid and of the reference stars to a common frame, resulting in a dominant contribution to the final uncertainty.

In order to ameliorate this problem, we modified our strategy in two ways. First, the number of available intermediate-brightness reference stars was a primary consideration in the selection of our targets. Second, we have obtained and processed serpentine scans in $F606W$; these scans provide additional constraints between the Cepheid, which is not saturated, and a larger number of intermediate-brightness reference stars. (Similar data were collected in some of the SY Aur epochs, but we were unable to process them properly for Paper 1.) Position measurements for intermediate and faint stars in serpentine scans are not quite as accurate as those in the straight $F606W$ scans, for a number of reasons: the same total counts are spread over a larger area, thus resulting in additional background noise; the higher density of trails results in more spoilers; and the more complex telescope motion results in additional parameters to be fitted. Nonetheless, we find that serpentine scans, while more complex to analyze, add significantly to the precision and reliability of the final measurement, and we expect that the analysis of future targets will use the serpentine scans as well.

To account for a shift in detector X position due to imperfect X-CTE, we have obtained calibration observations for WFC3/UVIS in spatial scan mode, in which a bright star has been moved across the amplifier boundary at $X = 2048$ in consecutive exposures. To the extent that the X-CTE effect is linear in the distance to the relevant amplifier, the mean relative position of stars in the field does not change as the field of view is dithered in the X direction—if stars are moved to the right ($+X$ direction), those to the left of the boundary ($X < 2048$) will experience an increase in their apparent displacement to the right, and those to the right of the boundary ($X > 2048$) will experience a *decrease* of their apparent displacement to the left, for a null net effect. (Individual stars will move slightly with respect to one another, as fainter stars will be affected more than brighter stars.) However, if a star is moved from left to right of the boundary, its apparent displacement due to X-CTE will reverse sign, and thus it will experience a large net motion. An analysis of

calibration observations obtained in Fall 2014 shows that the net effect is 8 mpix for a star near saturation, thus implying that a bright star near the amplifier boundary was shifted by 4 mpix at that time owing to X-CTE.

Experience with WFPC2, ACS, and (more limited) with WFC3/UVIS strongly suggests that CTE effects grow linearly with time in orbit and with distance to the relevant amplifier. For WFC3/UVIS, we assume that the CTE loss was zero at launch. If this is correct, and if the effect is furthermore anti-symmetric with respect to the amplifier boundary, the impact of X-CTE upon parallax determinations vanishes *as long as the observations are obtained with the same center and rotated field of view*. The reason is that a growing X-CTE will result in an apparent motion for each star which is indistinguishable from a proper motion; thus, each star will have a spurious term in its estimated proper motion, but the parallax estimate is unaffected. Even if the field of view is shifted, the impact on each star is minimal, as discussed above— as long as the star does not switch amplifiers.

However, second epoch observations placed the Cepheid at the same X detector location ($X \approx 2000$, left of the amplifier gap) as the odd epochs, thus shifting the field center by about 100 pixels between the two orientations. The aim was to minimize the impact of uncertainties in the geometric distortion for the Cepheid by placing it in approximately the same detector location. The magnitude of the X-CTE effect was not fully understood at that time. On the basis of current information, minimizing the impact of X-CTE effects is deemed more important, and starting from Epoch 3, observations were obtained with the same field center for all epochs.

In order to correct for the residual X-CTE effect—which generally only affects the Cepheid target, as other stars within 50 pixels of the amplifier boundary are swamped by the light of the target—we simply correct the position measured for the Cepheid in Epoch 2 by twice the estimated offset at that time, about 2.9 mpix. This correction mimics the effect of placing the Cepheid in the symmetrical position ($X \approx 2100$) and thus nullifies the effect of X-CTE on the measured parallax. As discussed above, relative proper motions *will* be affected by X-CTE and thus can only be determined accurately if a good overall calibration for X-CTE is obtained.

2.6.1. Serpentine Scans

Although in many ways the serpentine scans are treated similarly to the regular straight scans, some special considerations apply. For each leg, we exclude from the fit a region of about 300 pixels before and after each turning point, in which the motion of the telescope deviates significantly from a straight line. In principle, we could include this deviation in the overall fit; however, the local slope can be large enough that our underlying approximation that the scan direction is perpendicular to the resolution direction no longer fully applies. For such regions, the variable-rotation solution (see § 2.4) would also fail its underlying assumptions. Therefore, we simply ensure that we only include the portion of each leg where the mean displacement of the motion from a straight line is less than 0.1 pixels.

In addition, serpentine scans do not provide a good way to determine the start or end point of each leg accurately during the initial fit. The half-rise method does

not work, as each leg is truncated by the cutoff in the horizontal offset, rather than by the rise or fall due to the shutter. Only the very first and last leg could have a half-rise measurement, and only if the relevant start/end point occurs on chip. For this reason, we put special care in estimating the start and end point from the overall shape of the serpentine scan, and we use these start and end points for the initial guess at the vertical positioning of each scan. In keeping with our procedures for straight scans, a refinement step occurs in which a least-squares fitting of the jitter pattern along the scan is used to improve the relative positioning of each scan. This step works to a similar accuracy as for the straight scans, after taking into account the relative signal levels and scan lengths.

2.7. Combining Multi-Epoch Data: Toward a Parallax Measurement

For each epoch of observation, our goal is to obtain a measurement of the relative positions of all stars, the Cepheid as well as all the reference stars, along the resolution direction (the distortion-corrected detector X axis projected onto the sky). This measurement must be as accurate and free of systematics as possible.

In order to obtain a measurement of the relative parallax and proper motion (in the resolution direction) of the stars on the field, data from all available epochs must be combined. In addition, information on the distance of the reference stars is required in order to obtain an absolute parallax for the target. In principle, the process requires only a linear combination of the positions as measured at each epoch to determine relative parallaxes and proper motions; if the mean parallax of the reference stars can be estimated, determining the parallax of the target is then straightforward.

In practice, solving for the parallax of the target is much more complex. Small rotations (at the level of a few hundredths of a degree) between epochs, as well as small changes in plate scale and low-order geometric distortion which are known to occur, can substantially affect the projected positions of each star in each epoch, and thus impact significantly its estimates of parallax and proper motion. Occasionally, reference stars can have anomalous data, either because of measurement problems (e.g., undetected faint stars close enough to affect the fit), or for astrophysical reasons (e.g., binary companions or other sources of photocenter motion).

The approach we have adopted solves *simultaneously* for the astrometric parameters of all the stars in the field and for the geometric registration of all the epochs, using the spectrophotometric parallax estimates as priors for their astrometric parallax. With this approach, the spectrophotometric parallax estimates help constrain the registration between epochs, including the relative low-order geometric distortions. It is thus critical that the parallax estimates be as accurate and robust as possible.

In the next section, we present the combination of spectroscopic and photometric data and the analysis that leads to spectrophotometric distance estimates for as many of the reference stars as possible.

In § 4 we return to the determination of the Cepheid parallax using the spectrophotometric distance estimates obtained in § 3.

3. SPECTROPHOTOMETRIC DATA AND DISTANCE ESTIMATES

3.1. *Photometry and Spectroscopy of Reference Stars*

Narrow-angle astrometry, such as what we can obtain with *HST*, is fundamentally differential in nature, and therefore it can only constrain the *difference* between the parallax of stars within the field of interest. In order to convert this relative parallax estimate into an absolute measurement, the parallax of other stars in the field must be estimated, and careful consideration must be given to possible systematics and random uncertainties in these estimates. In addition, estimates of the parallaxes of other stars in the field can *confirm* the quality of the astrometric measurements, identify outliers, and help constrain some of the low-order geometric distortion variations discussed earlier.

For this reason, we have obtained multi-band photometry and medium-resolution, classification-quality spectroscopy for most likely reference stars in the field of SS CMa. A combination of stellar model fitting and spectrophotometric classification, together with an understanding of the distribution of stars along the line of sight, has been used to estimate the distance to each reference star and its likely uncertainty. We also used prior estimates of the reddening along the line of sight, based on measurements of stars in 2MASS and Pan-STARRS, in order to constrain the range of possible reddening; however, the final reddening-distance law was also fitted for in our analysis.

3.1.1. *Photometry for Reference Stars*

For the SS CMa field (and for other Cepheid fields in progress), we obtained direct imaging with *HST* during the scanning observations and measured photometry of all reference stars in the UV (*F275W*, *F336W*), Strömgren (*F410M*, *F467M*, *F547M*), and broad-band (*F850LP*) systems. In order to obtain the photometry efficiently within the observing time available to our program, we used 2×2 binned mode, in which full-field WFC3/UVIS images are binned on-board before being saved to the *HST* computer for download. In this mode, images have a substantially smaller memory footprint, and more images can be obtained before the instrument memory is full and the images must be transferred to the *HST* solid-state storage. Consequently, we were able to obtain several photometric measurements within each orbit, without impacting the scanning mode observations. We have developed and tested procedures to accurately recover and calibrate binned-mode photometry, and we obtained reliable photometry (albeit with larger uncertainties) even for partially saturated stars.

We also obtained *F160W* photometry with WFC3/IR, and we added *J*, *H*, and *K*-band photometry from the 2MASS survey, as well as Channel 1 and Channel 2 photometry from *WISE* when available, to provide a set of up to 14 bands of photometry from 0.2 to 4.5 μm . All of the photometry was of high signal-to-noise ratio, with the exception of *F275W* where only a third of the stars yielded a measurement ($F275W < 22.8$ mag). Missing or excluded photometry was recorded for stars which suffered cosmic ray hits, suffered blending in the 2MASS or *WISE* data (as identified from their data quality flags or from *HST F850LP* imaging), and for half the field not

covered by *F410M* imaging. The resulting photometric information is reported in Table 2.

3.1.2. *Spectroscopy of Reference Stars*

We independently determined the temperature and luminosity class of the majority of the reference stars via medium-resolution optical spectra compared to template spectra. As indicated in Table 2, spectra were obtained with the Kast double spectrograph (Miller & Stone 1993) on the 3 m Shane reflector at Lick Observatory, with GMOS on Gemini South (Hook et al. 2004), and with LRIS on Keck McCarthy et al. (1998). Standard procedures were used for the data reduction.

3.1.3. *Estimating Spectrophotometric Parallaxes*

Spectroscopic parallaxes of stars in the field were determined, as in Paper 1, by matching up to 14 bands of photometry to stellar isochrones, comparing medium-resolution spectroscopy to stellar spectra for classification standards, and using the Besançon Galaxy Model (Robin & Crézé 1986; Robin et al. 2003, and references therein) as a likelihood prior for stellar parameters. We used a version of the model with an updated thick disk which better fits Sloan Digital Sky Survey (SDSS) and 2MASS data (Robin 2013, private communication).

Our procedure for measuring the spectroscopic parallaxes of the astrometric reference stars in the field has been somewhat refined and improved since the procedure used for the field of SY Aurigae described in Paper 1. We have now added photometry of the stars from two bands of spatial scanning, a broad (*F606W*) and another Strömgren (*F621M*) filter, one broad band from *HST* in the NIR (*F160W*), and two bands of medium-IR data from the all sky *WISE* mission. We add an uncertainty of 0.05 mag in quadrature to all photometric uncertainties to account for possible differences in photometric systems between models and observations. The stellar classification of star temperature and luminosity class is now done using the MKCLASS version 1.7 automated Morgan-Keenan classifier (Gray & Corbally 2014). Finally, we have improved our prior knowledge of the extinction along the line of sight as a function of distance using the 2MASS determinations from Marshall et al. (2005), who provided extinction vs. distance estimates for the line of sight in the direction of SS CMA (private communication) with an uncertainty of 0.3 mag at a given distance. An example of the quality of the results is shown in Figure 11 for Star 18; the observed photometry (diamonds) is matched to a reddened model (dashed line), with the residuals shown on a larger scale in the bottom panel. The inset shows the observed spectrum for Star 18 (black) overlaid with the best-fitting model according to MKCLASS (red). Note that the

Because it can be difficult to estimate extinction along a line of sight at very low Galactic latitude, and because our up-to-14 band photometry stellar photometry spanning the 0.275 to 4.5 μm can aid the determination, we started with a weaker prior having a Gaussian width of 0.5 mag, and then, on the basis of the *a posteriori* extinction estimates, we applied a global correction to the 2MASS estimates before reverting to the 0.3 mag uncertainty for a final estimate. The maximum extinction we allowed in the fits was 1.2 times the total extinction to infinity along this line of sight estimated by Schlafly &

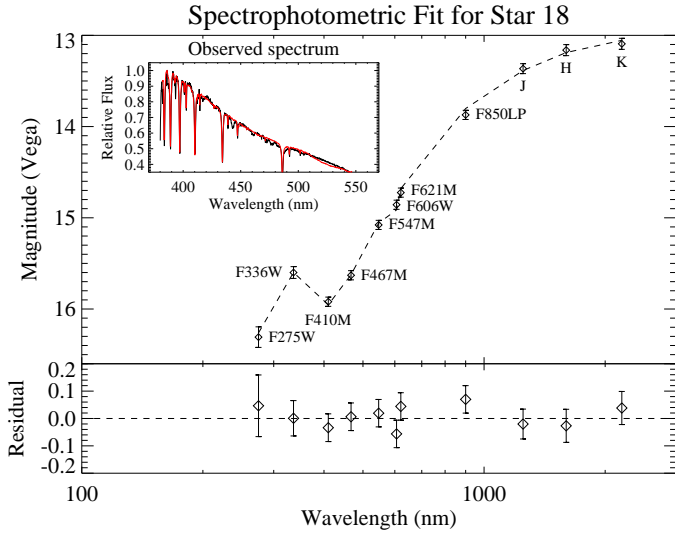


Figure 11. Spectral and photometric fit for the B2 V star 18. (Top panel) Observed photometry (diamonds) and best-fitting model from the Padova isochrones (dashed line). (Inset) The observed spectrum (black), continuum-corrected and fitted to a model spectrum (red) using MKCLASS. (Bottom panel) Residuals of the model photometric fit, shown on a larger vertical scale. Photometric errors include a 0.05 mag term added in quadrature to the measurement uncertainty to account for possible differences in photometric systems between models and observations.

Finkbeiner (2011), which in turn was based on a rescaling of the IRAS-based estimate of Finkbeiner et al. (1998). The scatter of the *a posteriori* extinction estimates for each star around the extinction prior at its (spectrophotometrically) estimated distance was 0.21 mag, with extinction values ranging from $A_V \approx 0$ at distance modulus $\mu = 9$ to $A_V = 3$ mag at $\mu = 13$. Figure 12 shows the resulting final law for A_V vs. μ (red points and red line), together with the individual values for each of the reference stars in the field (blue squares). The relation thus obtained between extinction and distance, for stars both closer and further away than the Cepheid, will also serve to constrain the reddening estimated for the Cepheid. This will in turn provide information on the intrinsic colors of the Cepheids and improve the robustness of the global P – L calibration we expect to obtain.

4. THE ABSOLUTE PARALLAX OF SS CMA

4.1. Multi-Epoch Combination and Parallax Fit

The final step in the astrometric solution consists of combining the multiple measurement epochs taken over the course of two years at intervals of six months to fit to our standard astrometric model which involves three parameters for each star: position, parallax, and proper motion along the measurement direction. The results we present here for SS CMA are based on five epochs of observation; four more epochs are being obtained as part of a recently approved program extension (Program GO-14206). The fifth epoch does not include the serpentine scan. The exposures used are listed in Table 3.

Together with the astrometric parameters of each star, the model includes up to second-order geometric parameters used to align each epoch with one another (offset and rotation), as well as any residual large-scale adjustment to the geometric distortion required to reduce the model residuals. This last part is identical to the single-epoch

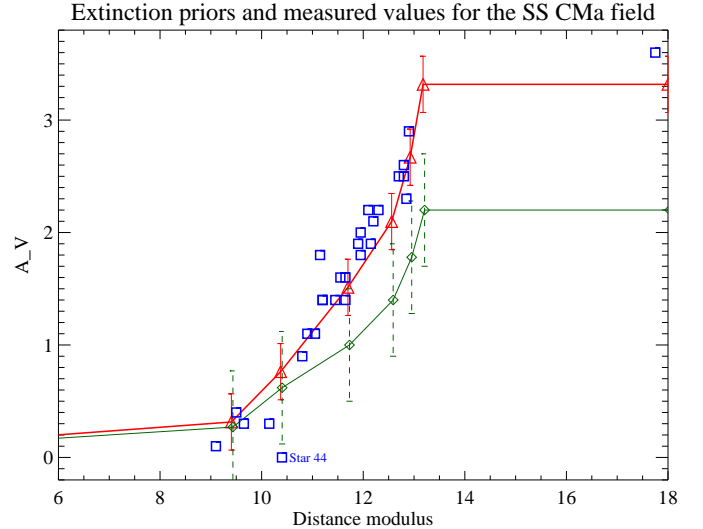


Figure 12. Estimated extinction vs. distance modulus for the SS CMA field. The green curve and values (diamonds with error bars) show the starting estimate of the relation between extinction and distance, which is iteratively adjusted during the fit process. The red curve and values (open triangles with error bars) shows the final relation. The blue squares show the estimated extinction for each of the reference stars with sufficient spectrophotometric information.

aggregation step, but it now substitutes the stationary-star assumption with the astrometric model for each star.

The full model can be formally described by the expression

$$X_{ij} = X_{i0} - X_{\text{ref},j} + PMx_i(t_j - t_0) + \pi_i f_j + R_j Y_{i0} + \langle P_j(X_{\text{det}}, Y_{\text{det}}) \rangle_{\text{trail}_i} \quad (1)$$

where the basic measurements are the positions X_{ij} —that is, the X position of the trail of star i in image j (relative to the reference scan line), measured after correction for variable rotation, scale-corrected for velocity aberration and variable distortion, and projected onto a constant sky frame. The X coordinate is aligned with detector X and, by design, aligned with the bulk of the parallactic motion. The quantity X_{i0} is the reference position of star i at time t_0 , and $X_{\text{ref},j}$ is the offset of image j in the X direction—in essence, the position of the reference scan line for image j on the sky. The astrometric motion of star i in the X direction is described by the X component of the proper motion, PMx_i , and the parallax π_i , applied with the epoch-dependent parallax factor f_j . The term f_j is the projection (for unit parallax) of the parallactic motion in the X direction at the time of the observations, computed using the formulae at pp. B28 and C5 of *The Astronomical Almanac* (2013), and the orientation of the detector axes from the image headers.

As we did for SY Aur, the model position must be corrected for the relative rotation and geometric distortion of image j with respect to the reference image. The rotation term on the sky is $R_j Y_{i0}$, where R_j is the rotation of image j and Y_{i0} is the static relative position of star i in rectified coordinates along the Y direction with respect to the center of the field. We find our rotations to be of order 10^{-5} , so even a coarse measurement of Y_{i0} with a precision of ~ 1 pixel will suffice. The polynomial term is determined simultaneously with the

astrometric parameters during the model-fitting procedure, as a second-degree $P_j(X_{\text{det}}, Y_{\text{det}})$, where X_{det} and Y_{det} are detector coordinates; the total correction is determined by evaluating the polynomial for image j at every location along the trail of star i in that image, and averaging the result. The constant term is omitted from the polynomial because it is degenerate with the image offset $X_{\text{ref},j}$.

Our proper motion term is relative to the set of stars in the field and contains a contribution from the estimated X-CTE term per year at that star’s location.

Note also that the model is formulated to be *linear* in the astrometric parameters, which in turn are linearly related to most measured quantities, i.e., positions on the detector. As a consequence, the errors in the derived astrometric parameters for the Cepheid are likely to be very nearly Gaussian (the same does not necessarily apply to distant stars for which the spectrophotometric constraints dominate the error distribution). As long as the parallax and its error distribution are used directly, there is no need to apply nonlinear correction such as those suggested by Lutz & Kelker (1973). More generally, proper consideration of all prior information used in selecting and characterizing the population of our target Cepheids will be required in determining the optimal calibration for the P - L relation on the basis of our measurements (Hanson 1979; Francis 2013; see also the discussion in Benedict et al. 2007). Therefore we do not include a Lutz-Kelker-type correction for the parallax of SS CMa at this point, but defer consideration of the proper characterization of the prior probability density function for our target to the analysis of the full sample of Cepheids.

As far as the astrometric model is concerned, parallaxes are also relative; however, the degeneracy in the conversion to absolute parallaxes can be broken by using the spectrophotometric distance estimates for the stars in the field discussed in § 3. The distance estimate of the target star will be insensitive to uncertainties in the distance of the reference stars so long as the set contains objects which are bright and distant (e.g., red giants). Note also that in addition to providing a conversion to absolute parallax, individual spectrophotometric parallaxes are also helpful in constraining some epoch-to-epoch geometric transformations. We will discuss in detail in § 4.2 the impact of the parallax constraints for reference stars on the multi-epoch solution, and investigate the consequences of uncertainties, outliers, and other possible issues.

Each epoch after the first is allowed a rotation, a net offset, and a second-degree polynomial adjustment to match the first epoch; since there are about 20 stars useful for measurement at each epoch, these additional 7 parameters per epoch over which we marginalize do not place an undue burden on the solution.

Formally, the *a priori* distance estimates based on spectrophotometric parallaxes serve as Bayesian priors for the parallax of the stars in the field. A prior is not used for the Cepheid, so that its distance estimate is determined directly and only from its observed parallax.

The best values of the model parameters are determined by minimizing the total model χ^2 to achieve the most likely parameters. Among these parameters is the *absolute* parallax of SS CMa, which results directly from

the model optimization. A modest fraction of the reference stars in the field are expected to be part of binaries with parameters that would cause a significant deviation from our simple astrometric model. This fraction depends on distance and spectral class, but is ~ 10 –20% for F and G stars at 1 kpc on the basis of the distribution of binary properties in Duquennoy & Mayor (1991, see also discussion in Paper 1). We run the global model iteratively after rejecting one outlier (Star n2) on the basis of its disproportionate contribution to the total χ^2 . We also exclude Star n10 because its astrometric parallax is suspect, resulting in a very large estimated distance which is inconsistent with its spectrophotometric information.

4.1.1. Multi-Parametric Model for SS CMa: Primary Solution

Figure 13 shows the best estimate of the parallax for the stars in the SS CMa field. For reference stars, the reported parallax combines both astrometric and spectrophotometric information; no spectrophotometric information is used for the Cepheid SS CMa (the star labeled 0).

For each star, the top panel shows the astrometric measurements at each epoch (dots with error bars) and the best-fitting parallax model (red line), both in milliarcseconds; the fitted proper motion is subtracted from both measurements and model for ease of display. The gray band shows the spectrophotometric parallax estimate with a 2σ uncertainty, when available. The bottom panel shows the astrometric residuals from the best model, also in milliarcseconds.

The best estimate of the parallax of SS CMa is 0.348 ± 0.038 mas, corresponding to a distance estimate of 2.87 ± 0.33 kpc. However, note that, as commented in § 4.1, the error distribution is likely Gaussian *only in parallax*. A nonlinear conversion, e.g., to distance, will have a nonsymmetric error distribution, which must be taken into account in further processing. It is also necessary to consider any prior information used in selecting and characterizing the sample (Hanson 1979; Francis 2013; see also the analysis in (Benedict et al. 2007).

The uncertainty in the conversion to absolute parallax (i.e., the systematic uncertainty in the frame parallax) of the set of 20 fitted reference stars is $7 \mu\text{as}$, well below our target uncertainty. In the field of SS CMa, the precision of the conversion to absolute parallax benefits from the presence of some very distant stars, and especially Star 43, whose spectrophotometry indicates that it is a K giant at around 30 kpc (§ 4.3). However, even excluding Star 43, the rest of the reference stars indicate an uncertainty in the frame parallax of about $11 \mu\text{as}$, still much smaller than our target uncertainty. This is not surprising; Fig 14 shows the typical precision of the correction to absolute parallax in random fields generated from the Besançon model for the direction of SS CMa, assuming a 15% typical uncertainty in spectrophotometric distance estimates and that only half of the stars in the field will be available for the conversion. A typical field would have ~ 20 available reference stars and an uncertainty of $9 \mu\text{as}$ in the conversion to absolute parallax for an assumed RMS uncertainty of 0.3 mag in the estimated distance moduli, comparable to the values for the actual data. (The uncertainty in the conversion to abso-

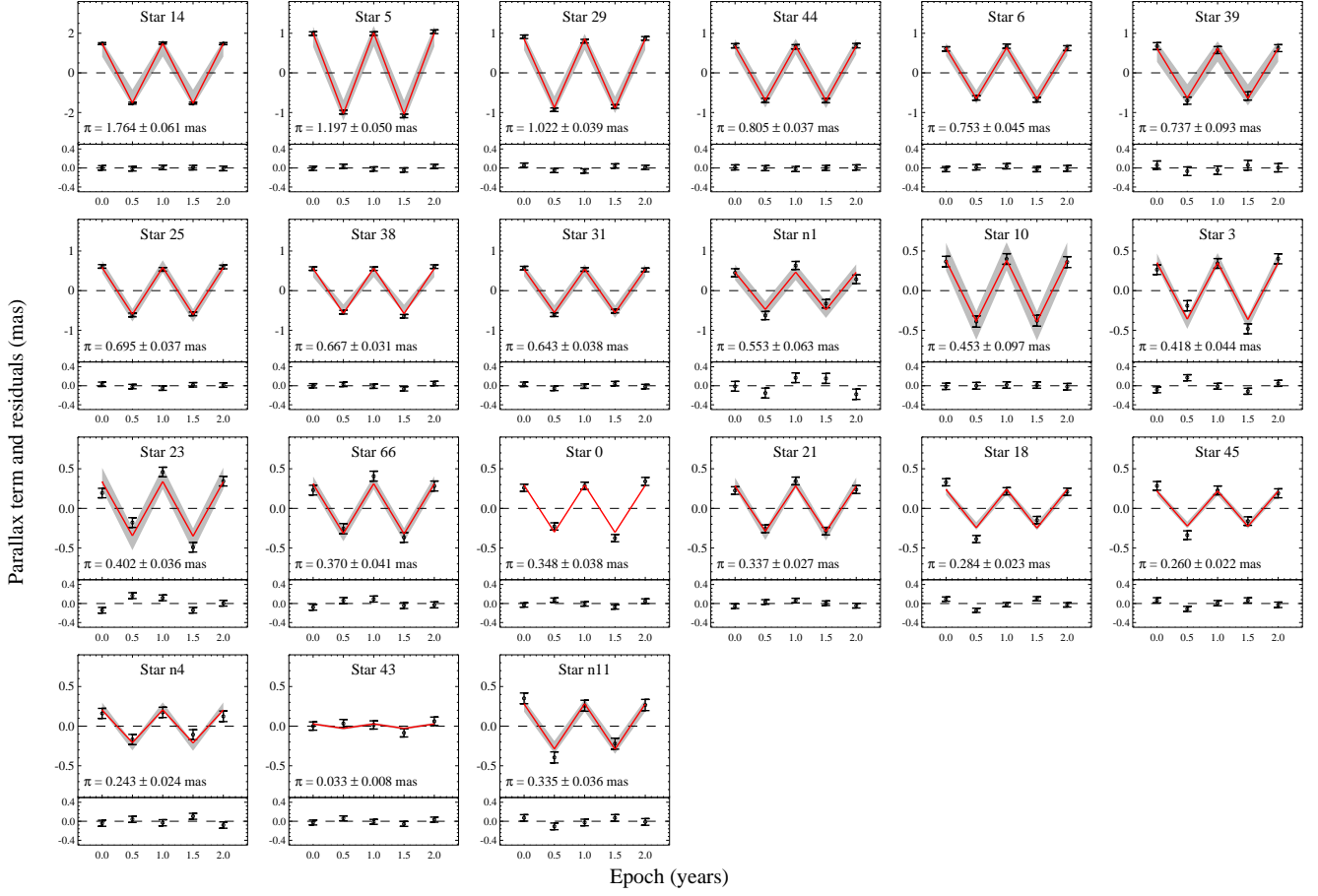


Figure 13. Individual stellar parallaxes in the field of SS CMA. The red line indicates the measured parallax; the grey band indicates the spectrophotometric parallax with $\pm 2\sigma$ width. The Cepheid SS CMA is Star 0. Fitted proper motions have been subtracted from the measurements and fits for ease of viewing. Star 29, the putative companion of the Cepheid, is much closer to the Sun and is not physically associated with it.

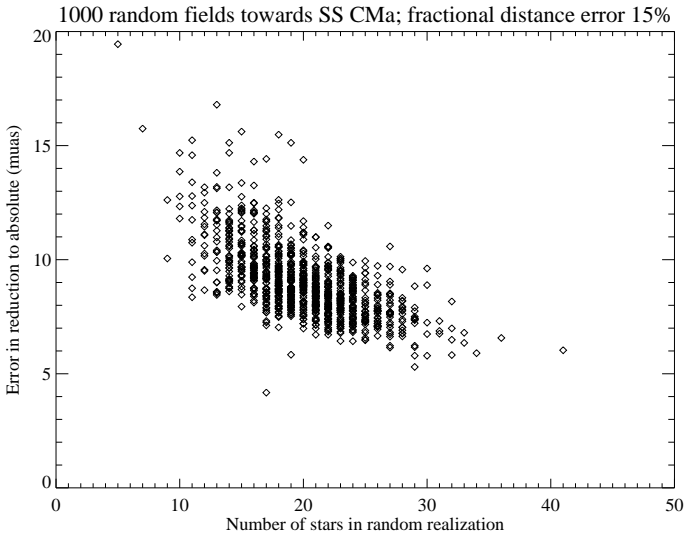


Figure 14. Distribution of expected errors in the conversion to absolute parallax for 1000 fields drawn randomly from the Besançon model in the direction of SS CMA. We assume that only half the stars in each field are available as reference stars, and that each has a 15% error in its spectrophotometric distance estimate (about 0.3 mag in the estimated absolute magnitude). Typical values are $9 \mu\text{as}$ for ~ 20 stars, consistent with the actual values for our field when Star 43 is excluded.

lute scales roughly linearly with the assumed uncertainty

in the distance moduli.) However, Star 43 is unusual in its own right, and will be further discussed in § 4.3.

4.2. Astrometric vs. Spectrophotometric Parallax; Partially-Constrained Solutions

In the primary solution, we assumed that the spectrophotometric and astrometric distance estimates for each star are separate but valid measurements of the same quantity, the physical distance of each star. In practice, this assumption may not always be true, e.g., because of the possible binarity discussed earlier. On the other hand, the assumptions underlying our spectrophotometric distance estimates may not be valid for all stars, and there could be outliers—e.g., due to anomalous extinction, or a history of mass exchange—which could occasionally lead to a faulty estimate of the distance modulus.

A careful comparison of astrometric and spectrophotometric parallaxes for the reference stars can provide a powerful check of our procedures and our final accuracy. Spectrophotometric parallaxes, derived from a combination of spectra and multiband photometry in conjunction with stellar model tracks, a model of the density distribution of stars along the line of sight, and an extinction model, typically have fractional accuracy that varies little as a function of distance; thus, their absolute error is much smaller for distant stars than for nearby ones.

On the other hand, astrometric parallaxes have absolute errors that are similar in magnitude in terms of parallax angle, and hence nearly independent of distance, although they do scale with apparent brightness; thus, for nearby stars, astrometric parallaxes are more accurate than spectrophotometric ones, and vice versa for distant stars. For typical stars in our analysis, the two accuracies are comparable at about 1 kpc. Consequently, stars beyond 1 kpc provide a solid check of astrometric measurements, while closer stars provide a verification of the spectrophotometric estimates.

However, the parallax estimated for each star in the full (primary) solution shown in Figure 13 is affected by its spectrophotometric prior, and hence cannot be used directly for an independent check of the astrometric parallax thus obtained. On the other hand, dropping all of the spectrophotometric priors is not a viable option. First, all narrow-field parallax measurements are, by necessity, only relative; thus, without *some* spectrophotometric measurements, no absolute parallax can be derived. Second, as discussed in § 4.1, without a spectrophotometric prior for the majority of the stars, we lack the ability to properly constrain the relative alignment and polynomial distortion for each epoch of observation, thus worsening the quality of the measurements and introducing substantial degeneracies in the solution process.

In order to carry out a meaningful test of the quality of our astrometric parallaxes, we repeat the multi-epoch fit by discarding the spectrophotometric prior for each star in turn, and define the parallax obtained for that star as its *pure astrometric* parallax. For example, when measuring the pure astrometric parallax for Star 29, we discard the spectrophotometric prior *only for Star 29*, but retain the prior for all the other stars in the field that have one. This allows the solution to converge with only a minor decrease in overall precision, resulting in a trigonometric parallax estimate to Star 29 that is completely independent of any photometric or spectroscopic information for that star. We call this the “pure” astrometric parallax, and list it as π_{astro} in Table 2, where the parallax resulting from the full solution is labeled π_{full} . We then repeat this process for all other stars for which a spectrophotometric prior is available; for stars without a spectrophotometric prior, including the Cepheid, the pure astrometric parallax is of course identical to the parallax from the full solution. This procedure not only allows us to assess the quality of our astrometric measurements with the spectrophotometric distance estimates, but also mimics the handling of the Cepheid itself, for which no spectrophotometric prior is ever used, and thus provides a useful test of the validity of its parallax measurement.

Figure 15 shows a comparison of the pure astrometric and spectrophotometric parallaxes for the reference stars in the field of SS CMa. The Cepheid is not included, as no spectrophotometric prior is used for it. For the majority of the stars, there is a very reasonable agreement between them, with 17 out of 20 within nominal 2σ ; only stars 3, 38, and n4 are outside this range, and Star 10 has a very small value for the pure astrometric parallax, with a very large uncertainty.

Excluded from Figure 15 is Star n10, for which the pure astrometric parallax is negative. In our solution, “nega-

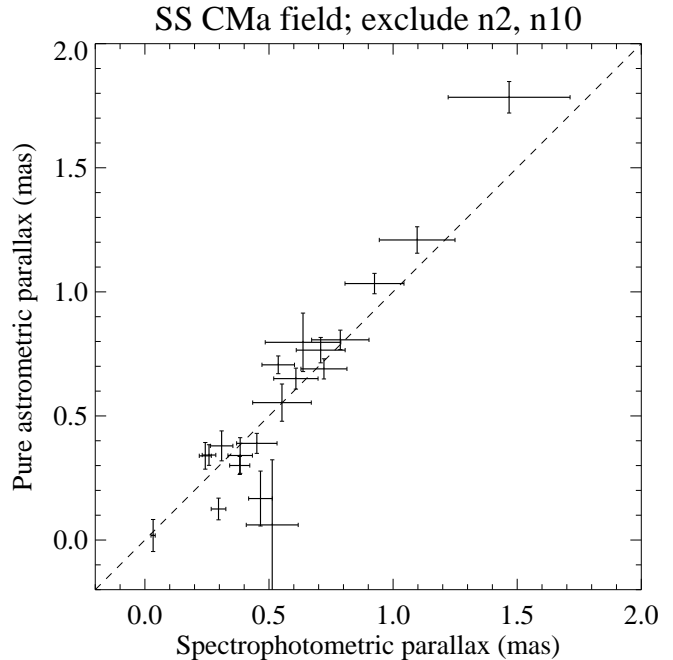


Figure 15. Comparison between spectrophotometric and pure astrometric parallax, obtained by excluding the spectrophotometric prior for each star in turn. Therefore, the pure astrometric parallax for each star is solely based on its astrometric measurements, and is not affected by any spectroscopic or photometric data for that star.

“negative” parallaxes are not necessarily disallowed; they can occur, for example, if the correction to absolute parallax is underestimated, and all stars are in reality closer than the astrometric parallax indicates. In that case, the true parallax would simply be larger than the resulting value, because of the larger correction to absolute parallax. However, in this case the solid agreement between astrometric and spectrophotometric parallaxes for most stars argues strongly against a large systematic error in the reduction to absolute parallax. Although we could limit the solution to require *positive* parallaxes, this step would be somewhat arbitrary, given that the actual value of the reference parallax is part of the optimization process, and could give excessive weight to stars with very low parallaxes in the solution. Therefore we treat Star n10 as an astrometric outlier and exclude it from our solution. Based on the discussion in Paper 1, we expect $\sim 10\%$ of the reference stars to be astrometric outliers due to binarity, so the presence of an outlier in this sample is not surprising.

It is important to note that the accuracy of the partially constrained solutions obtained by dropping the spectrophotometric prior for one of the reference stars can be potentially compromised, especially if that star is near a corner of the field. The reason is that the low-order polynomial distortion that we adopt to register the measurements across epochs may lack a critical constraint near that corner, while on the other hand its *value* is required at that location. Consequently, a quasi-degeneracy in the multi-epoch astrometric solution exists for that star. This is especially apparent for stars such as Star 3, which is the only bright star near the bottom left of the field (see Fig. 3). The full solution (Fig. 13) shows for Star 3 a normal parallax value and uncertainty

of 0.418 ± 0.044 mas, and its residuals are fairly typical. On the other hand, the partially constrained solution in which its parallax prior is dropped is 0.167 ± 0.111 mas, with a very different value and a much larger uncertainty than the fully constrained solution. Inspection of the two solutions shows that they differ by about 40% in the Y^2 polynomial term, resulting in a differential offset of up to 10 mpix in Epoch 5. The case of Star 10 is even more extreme, with an increase of the nominal error from 0.096 mas to 0.260 mas for the pure astrometric parallax. For most other stars, the uncertainty increases by 10–70% when the spectroscopic prior is dropped. (Another exception is Star 43, which has a comparatively poor fractional accuracy in the trigonometric parallax because of its very large distance.) Figure 16 shows the difference between pure astrometric and spectrophotometric parallax as a function of distance from the center of the field: two of the three stars with difference larger than 0.3 mas are more than 2000 pixels from the field center.

In summary, we conclude that there is in general good consistency between the astrometric parallaxes we measure from this set of *HST* spatial scans and the distance estimates obtained from our spectroscopic and multiband photometric measurements. Moreover, as expected, the availability of such estimates for a large fraction of the reference stars is necessary to constrain the overall astrometric solution.

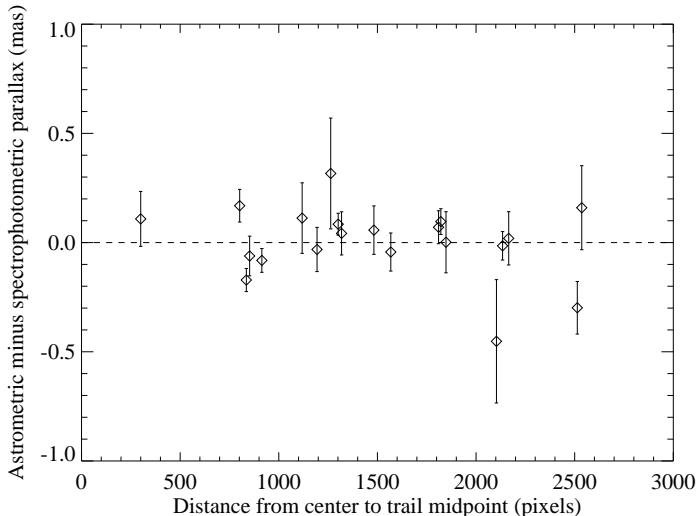


Figure 16. Difference between spectrophotometric and pure astrometric parallax, plotted as a function of the distance of each star from the field center. The error bars combine in quadrature the uncertainties in both parallaxes. The largest deviations occur for stars far from the center of the field, reflecting the difficulty in constraining the polynomial distortion terms when the stars at the edge of the field (which have the most leverage) are excluded from the prior.

4.3. Two Special Reference Stars

Among the reference stars in the field, Star 29 was suggested by Evans & Udalski (1994) as a possible binary companion to SS CMa, on the basis of its blue color, estimated distance, and likelihood of the relatively small separation of $13''$. However, we classify Star 29 as G6 V on the basis of its spectrum (see Table 2), and its estimated

spectrophotometric distance modulus is 10.2 ± 0.3 mag, which places it significantly closer than the Cepheid. As shown in Figure 16, the astrometric parallax is in agreement, and we conclude that Star 29 is **not** physically associated with the Cepheid SS CMa.

Another interesting reference star is Star 43. Although faint in the visible ($V_{606} = 15.26$ mag), this star is quite bright in the NIR ($H = 10.76$ mag), and is classified from the spectrum as a K5 III, with spectrophotometric distance modulus 17.4 ± 0.5 mag. This places the star about 30 kpc from the Sun, well outside the disk and the spheroid of the Galaxy. (Note that this star by itself carries about half the weight of the conversion to absolute parallax for this field.) The trigonometric parallax without spectroscopic prior is 0.018 ± 0.065 mas, hence not significantly detected, but certainly indicative of the star being beyond 10 kpc. Such stars are likely rare, and are often found through variability studies or special spectral features (see, e.g., the carbon-star selection in Huxor & Grebel 2015). The Besançon model (Robin & Crézé 1986; Robin et al. 2003, and references therein) indicates that only one in fifty fields at the Galactic coordinates of SS CMa would have a star of comparable brightness beyond 10 kpc, and about one in 150 beyond 30 kpc.

5. LIMITS ON BINARITY FROM RADIAL VELOCITY OBSERVATIONS

As mentioned in § 2.2, there have been suggestions in the literature that SS CMa might be a binary, either from the properties of a nearby star (Star 29 in our list) or from variations of the measured RV. In general, binarity can affect the estimated astrometric parallax if the orbital motion of the Cepheid has a significant component in common with the parallactic motion. Over the short time span of our observations (~ 2 years, with 6-month sampling), periods between a few months and 3 years could have a significant impact on the measured parallax, if the orbital motion is of sufficient amplitude and oriented appropriately. We can rule out that Star 29 is a binary companion on the basis of both its spectrophotometric and astrometric parallax; even if it were physically associated with SS CMa, its impact on the parallax would be negligible owing to the extremely long inferred period. On the other hand, a spectroscopic binary companion could in principle impact the astrometric measurement. *A priori* considerations on the likelihood of binarity as a function of period and mass ratio (see Paper 1) suggest that the probability of a significant effect (larger than $10 \mu\text{as}$) is $\sim 10\%$, but these estimates are based primarily on binary statistics obtained for lower-mass stars (see, e.g., Duquennoy & Mayor 1991), and thus their applicability to massive Cepheids is uncertain. However, in the case of Cepheids, RV measurements can provide useful *direct* limits on the possibility of binarity and its impact on the measured parallax.

5.1. Spectroscopic Data

We observed SS CMa between April 2013 and November 2015 using three different echelle spectrographs: (1) the Hamilton spectrograph (Vogt 1987) at the Shane 3 m telescope located at Lick Observatory; (2) the Hermes spectrograph (Raskin et al. 2011) at the Flemish 1.2 m Mercator telescope located at the Roque de los Mucha-

chos Observatory on the island of La Palma, Spain; and (3) the Coralie spectrograph (Queloz et al. 2001) at the Swiss 1.2 m Euler telescope located at La Silla Observatory, Chile. Data from the Hermes and Coralie spectrographs were reduced using dedicated pipelines. Hamilton spectra were reduced using standard IRAF routines. RVs were determined by cross-correlation using a numerical mask representative of a solar spectral type (Baranne et al. 1996; Pepe et al. 2002).

RVs from Hermes and Coralie were found to be compatible with each other to within 10–20 m s^{-1} , and no zero-point offset was applied. RVs from the Hamilton spectrograph were brought to the Coralie/Hermes zero-point via observations of stable standard stars (HR 4027 and one or more of the following: HD 26161, HR 124, HR 7373, or NSV 7543) using the velocities and zero-point offsets presented by Nidever et al. (2002). Given the uncertainties involved with this zero-point correction, and factoring in the intrinsic precision of the Hamilton RVs, we estimate an uncertainty of approximately 200 m s^{-1} for these data. The individual pipeline-estimated RV uncertainties for Coralie and Hermes range between 20 and 80 m s^{-1} . We opt to not include the literature RV data from Joy (1937) and Coulson & Caldwell (1985) in this analysis, since zero-point offsets ($1 \pm 0.5 \text{ km s}^{-1}$ for Coulson & Caldwell 1985) and low precision (typical uncertainties larger than 1 km s^{-1}) dilute the precision of our new measurements, while not adding significant information for the timescales of interest (1–2 years).

5.2. Analysis

To investigate a possible astrometric signal caused by binarity, we constrain possible values of the projected semimajor axis, $a_1 \sin i$, for SS CMa by modeling the RV data. Our model consists of a sum of a 9-harmonic Fourier series, representing the intrinsic velocity variation during the pulsation, and a circular orbital motion. We adopt circular orbital motion for simplicity, and since there is no evidence for an eccentric orbit in the available data. We adopt a constant pulsation period of $P = 12.3535$ days, which minimizes the scatter in the phased RV dataset. We then convert the projected semimajor axis into an astrometric term by assuming a distance of 3 kpc. As usual with RV information, this represents a *minimum* orbital signature, corresponding to an edge-on orbit.

The time sequence of RV measurements indicates a nearly constant systemic RV, excluding even fairly low-amplitude deviations (above $\sim 400 \text{ m s}^{-1}$), consistent with a null detection of orbital motion to within the uncertainty of our measurements. We estimate upper limits on astrometric signals caused by undetected companions, noting that small variations in the pulsation RV pattern already found in several Cepheids (Anderson 2014b) can mimic the effect of low-mass spectroscopic companions (Anderson et al. 2015). Hence, the mere detection of time-variable low-amplitude changes in systemic velocity is not necessarily a clear indication of spectroscopic binarity, as the available sampling of the RV data is insufficient to fully separate these two possibilities. If interpreted as orbital motion, the variation seen in the RV data would result in the astrometric signature shown in Figure 17; darker colors correspond to lower χ^2 . The

maximum impact is around a period of 1 year with an orbital amplitude of $\sim 4 \mu\text{as}$, while the lowest χ^2 occurs for an amplitude of $1.5 \mu\text{as}$. In order to account for the uncertain contribution of the possible orbital motion, we conservatively add a term of $4 \mu\text{as}$ in quadrature to the nominal parallax error for SS CMa. Monitoring of this and other Cepheids in our program will continue, and the results will be presented separately in greater detail (Anderson et al. in prep.).

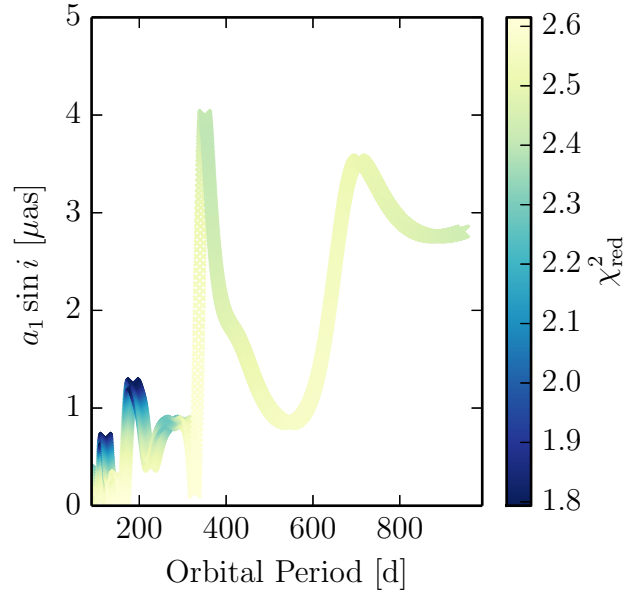


Figure 17. Best-fitting projected semimajor axis as a function of period for the RV data collected for SS CMa. The amplitude shown here assumes that all the variation in RV is due to orbital motion; in reality, variations in the RV profile during pulsation are likely to contribute substantially to the apparent RV variation, as shown by the fact that the reduced χ^2 remains above 1.8 throughout. The color corresponds to the value of the reduced χ^2 , with darker colors corresponding to better models. The largest possible impact on the astrometric parallax measurement is for an orbital period ~ 1 year, and is approximately $\pm 4 \mu\text{as}$; however, a shorter period with a much smaller astrometric impact ($< 1.5 \mu\text{as}$) is more consistent with the RV measurements.

6. DISCUSSION

We have presented a trigonometric parallax estimate for SS CMa, the first of 18 Galactic Cepheids in our program of measurements to obtain an improved calibration of the period-luminosity relation of Cepheids with properties comparable to those we are discovering in hosts of Type Ia supernovae within 35 Mpc. The parallax of SS CMa is $0.348 \pm 0.038 \text{ mas}$.

Unlike the pilot case of SY Aur, presented in Paper 1, the availability of several bright reference stars and improvements in our analysis procedures result in a formal uncertainty comparable with the pre-observation expectations of 30–40 μas . Several of the improvements indicated in Paper 1 have been implemented for this and all other Cepheids in the sample. For example, we use two shallow and two deep scans at each epoch, we obtain serpentine scans for most epochs, and we have developed and adopted an improved geometric solution that removes a significant fraction of the static (“pattern”) difference between observations obtained at different roll

angles. We also have been able to quantify and correct for the effect of CTE losses in the detector X direction (X-CTE), although we discovered that the second-epoch observations were not obtained in an optimal position to minimize the X-CTE effect. All of these improvements will be applied to the remaining Cepheids.

In the near term, we expect to complete the five-epoch observations and analysis for the remaining 17 Cepheids in our sample. If we can achieve a comparable accuracy for the other Cepheids, we expect that the overall characterization of the period-luminosity relation *exclusively from our parallaxes* will yield an uncertainty in the distance-scale calibration of $\sim 2\%$, providing a powerful and independent test of the present distance scale (Riess et al. 2011). When combined with improvements in the calibration of the distance of NGC 4258, the contribution of the anchor distance to the calibration of H_0 is likely to drop to 1.5%. For a subset of 9 Cepheids, we will obtain an additional 4 epochs of observations, which we expect to further reduce the final calibration uncertainty, especially by improving our ability to identify and exclude outliers and learn more about the properties of the telescope.

Additional improvements may result from a simultaneous consideration of the data for *all* Cepheids. For example, there may be regularities in the long-term behavior of the geometric distortion of the instrument, which we now treat as an unknown term to fit for and subtract. If such regularities prove amenable to a global solution, we may be able to reduce the uncertainty in the final solution by as much as 30%.

In a parallel effort, we are also doubling the sample of nearby Type Ia supernova hosts for which Cepheids are being measured and characterized (Riess et al., in prep.). With this two-pronged approach, we expect to reduce the uncertainty in the *local* Cepheid-based measurement of H_0 by $> 40\%$ with respect to Riess et al. (2011). The culmination of the Cepheid-based efforts to refine the local measurement of H_0 will come with the final results from the *Gaia* mission (circa 2022), which could permit, when combined with larger samples of Type Ia supernova hosts, a measurement with accuracy of $\sim 1\%$ or better.

This project was enabled by significant assistance from a wide variety of sources. Merle Reinhardt, George Chapman, William Januszewski, and Ken Sembach provided help with the *HST* observations. We thank Ed Nelan, Matt Lallo, Fritz Benedict, and Barbara McArthur for productive discussions about the behavior of the FGS. We also thank Leo Girardi, Alessandro Bressan, and Paola Marigo for the use of and assistance with their Padova isochrone database, Anne Robin for assistance with the Besançon Galaxy Model, Eddie Schlafly and D. Marshall for input on the extinction along the line of sight to SS CMa, and Nolan Walborn for useful discussions on the classification of hot stars.

Support for this work was provided by NASA through programs GO-12679 and GO-13101 from the Space Telescope Science Institute, which is operated by AURA, Inc., under NASA contract NAS 5-26555. A.V.F.'s group at UC Berkeley is also grateful for financial assistance from NSF grant AST-1211916, the TABASGO Foundation, and the Christopher R. Redlich Fund.

R.I.A. acknowledges funding from the Swiss National Science Foundation as a postdoctoral fellow. S.C. and A.G.R. gratefully acknowledge support by the Munich Institute for Astro- and Particle Physics (MIAPP) of the DFG cluster of excellence ‘‘Origin and Structure of the Universe’’. Research at Lick Observatory is partially supported by a generous gift from Google.

This research is based primarily on observations with the NASA/ESA *Hubble Space Telescope*, obtained at the Space Telescope Science Institute, which is operated by AURA, Inc., under NASA contract NAS 5-26555. Some of the data presented herein were obtained at the W. M. Keck Observatory, which is operated as a scientific partnership among the California Institute of Technology, the University of California and the National Aeronautics and Space Administration. The Observatory was made possible by the generous financial support of the W.M. Keck Foundation. Radial velocity measurements are based on observations taken with the Coralie echelle spectrograph mounted to the Swiss 1.2 m Euler telescope located at La Silla Observatory, Chile, and with the Mercator Telescope, operated on the island of La Palma by the Flemish Community, at the Spanish Observatorio del Roque de los Muchachos of the Instituto de Astrofísica de Canarias. The Euler telescope is supported by the Swiss National Science Foundation. Hermes is supported by the Fund for Scientific Research of Flanders (FWO), Belgium, the Research Council of K.U. Leuven, Belgium, the Fonds National de la Recherche Scientifique (F.R.S.-FNRS), Belgium, the Royal Observatory of Belgium, the Observatoire de Genève, Switzerland, and the Thüringer Landessternwarte, Tautenburg, Germany. We thank all observers who contributed in collecting the ground-based data used in this work, as well as the Euler and Mercator teams for their support.

This publication makes use of data products from the *Wide-field Infrared Survey Explorer (WISE)*, which is a joint project of the University of California, Los Angeles, and the Jet Propulsion Laboratory/California Institute of Technology, funded by NASA. It has also made use of the SIMBAD database, operated at CDS, Strasbourg, France.

REFERENCES

- Addison, G. E., Huang, Y., Watts, D. J., et al. 2015, ArXiv e-prints, arXiv:1511.00055
- Anderson, J. 2014a, The Impact of x-CTE in the WFC3/UVIS detector on Astrometry, Tech. rep.
- Anderson, J., & Bedin, L. R. 2010, PASP, 122, 1035
- Anderson, R. I. 2014b, A&A, 566, L10
- Anderson, R. I., Mérand, A., Kervella, P., et al. 2015, ArXiv e-prints, arXiv:1511.07089
- Baranne, A., Queloz, D., Mayor, M., et al. 1996, A&AS, 119, 373
- Bellini, A., Anderson, J., & Bedin, L. R. 2011, PASP, 123, 622
- Benedict, G. F., McArthur, B. E., Franz, O. G., Wasserman, L. H., & Henry, T. J. 2000, AJ, 120, 1106
- Benedict, G. F., McArthur, B. E., Franz, O. G., et al. 2001, AJ, 121, 1607
- Benedict, G. F., McArthur, B. E., Fredrick, L. W., et al. 2002, AJ, 123, 473
- Benedict, G. F., McArthur, B. E., Feast, M. W., et al. 2007, AJ, 133, 1810
- Benedict, G. F., McArthur, B. E., Napiwotzki, R., et al. 2009, AJ, 138, 1969
- Benedict, G. F., McArthur, B. E., Feast, M. W., et al. 2011, AJ, 142, 187

- Bennett, C. L., Larson, D., Weiland, J. L., & Hinshaw, G. 2014, *ApJ*, 794, 135
- Bennett, C. L., Larson, D., Weiland, J. L., et al. 2013, *ApJS*, 208, 20
- Coulson, I. M., & Caldwell, J. A. R. 1985, *South African Astronomical Observatory Circular*, 9, 5
- de Bruijne, J. H. J., Rygl, K. L. J., & Antoja, T. 2015, *ArXiv e-prints*, arXiv:1502.00791
- Duquenooy, A., & Mayor, M. 1991, *A&A*, 248, 485
- Evans, N. R., & Udalski, A. 1994, *AJ*, 108, 653
- Finkbeiner, D. P., Schlegel, D. J., & Davis, M. 1998, in *Lecture Notes in Physics*, Berlin Springer Verlag, Vol. 506, IAU Colloq. 166: The Local Bubble and Beyond, ed. D. Breitschwerdt, M. J. Freyberg, & J. Truemper, 367–370
- Francis, C. 2013, *MNRAS*, 436, 1343
- Freedman, W. L., & Madore, B. F. 2010, *ARA&A*, 48, 673
- Freedman, W. L., Madore, B. F., Gibson, B. K., et al. 2001, *ApJ*, 553, 47
- Gray, R. O., & Corbally, C. J. 2014, *AJ*, 147, 80
- Hanson, R. B. 1979, *MNRAS*, 186, 875
- Hershey, J. L., & Taff, L. G. 1998, *AJ*, 116, 1440
- Hoffmeister, C. 1929, *Astronomische Nachrichten*, 236, 233
- Hook, I. M., Jørgensen, I., Allington-Smith, J. R., et al. 2004, *PASP*, 116, 425
- Hu, W. 2005, *Phys. Rev. D*, 71, 047301
- Hubble, E. 1929, *Proceedings of the National Academy of Science*, 15, 168
- Humphreys, E. M. L., Reid, M. J., Moran, J. M., Greenhill, L. J., & Argon, A. L. 2013, *ApJ*, 775, 13
- Huxor, A. P., & Grebel, E. K. 2015, *MNRAS*, 453, 2653
- Joy, A. H. 1937, *ApJ*, 86, 363
- Kodric, M., Riffeser, A., Seitz, S., et al. 2015, *ApJ*, 799, 144
- Livio, M., & Riess, A. G. 2013, *Physics Today*, 66, 41
- Lutz, T. E., & Kelker, D. H. 1973, *PASP*, 85, 573
- MacConnell, D. J., Osborn, W. H., & Miller, R. J. 1997, *AJ*, 114, 1268
- Marshall, D. J., Robin, A. C., Reylé, C., & Schultheis, M. 2005, in *ESA Special Publication*, Vol. 576, *The Three-Dimensional Universe with Gaia*, ed. C. Turon, K. S. O’Flaherty, & M. A. C. Perryman, 135
- McCarthy, J. K., Cohen, J. G., Butcher, B., et al. 1998, in *Society of Photo-Optical Instrumentation Engineers (SPIE) Conference Series*, Vol. 3355, *Optical Astronomical Instrumentation*, ed. S. D’Odorico, 81–92
- Michalik, D., & Lindgren, L. 2015, *ArXiv e-prints*, arXiv:1511.01896
- Miller, J. S., & Stone, R. P. S. 1993, , *Tech. rep.*
- Mora, A., Bastian, U., Biermann, M., et al. 2014, in *EAS Publications Series*, Vol. 67, *EAS Publications Series*, 65–68
- Nelan, E. P., & Bond, H. E. 2013, *ApJ*, 773, L26
- Ngeow, C.-C., Kanbur, S. M., Neilson, H. R., Nanthakumar, A., & Buonaccorsi, J. 2009, *ApJ*, 693, 691
- Nidever, D. L., Marcy, G. W., Butler, R. P., Fischer, D. A., & Vogt, S. S. 2002, *ApJS*, 141, 503
- Oosterhoff, P. T. 1935, *Harvard College Observatory Bulletin*, 900, 9
- Pepe, F., Mayor, M., Galland, F., et al. 2002, *A&A*, 388, 632
- Perryman, M. 2009, *Astronomical Applications of Astrometry: Ten Years of Exploitation of the Hipparcos Satellite Data* (Cambridge University Press)
- Planck Collaboration, Ade, P. A. R., Aghanim, N., et al. 2015, *ArXiv e-prints*, arXiv:1502.01589
- Prusti, T. 2012, *Astronomische Nachrichten*, 333, 453
- Queloz, D., Mayor, M., Udry, S., et al. 2001, *The Messenger*, 105, 1
- Raskin, G., van Winckel, H., Hensberge, H., et al. 2011, *A&A*, 526, A69
- Reid, M. J., & Honma, M. 2014, *ARA&A*, 52, 339
- Riess, A. G., Casertano, S., Anderson, J., MacKenty, J., & Filippenko, A. V. 2014, *ApJ*, 785, 161
- Riess, A. G., Macri, L., Casertano, S., et al. 2009, *ApJ*, 699, 539
- . 2011, *ApJ*, 730, 119
- Robin, A., & Crézé, M. 1986, *A&A*, 157, 71
- Robin, A. C., Reylé, C., Derrière, S., & Picaud, S. 2003, *A&A*, 409, 523
- Sandage, A., Tammann, G. A., & Reindl, B. 2004, *A&A*, 424, 43
- Sandage, A., Tammann, G. A., Saha, A., et al. 2006, *ApJ*, 653, 843
- Schlafly, E. F., & Finkbeiner, D. P. 2011, *ApJ*, 737, 103
- Skrutskie, M. F., Cutri, R. M., Stiening, R., et al. 2006, *AJ*, 131, 1163
- Szabados, L. 1996, *A&A*, 311, 189
- van Altena, W. F., Lee, J. T., & Hoffleit, E. D. 1995, *The general catalogue of trigonometric [stellar] parallaxes*
- van Leeuwen, F., Feast, M. W., Whitelock, P. A., & Laney, C. D. 2007, *MNRAS*, 379, 723
- Vogt, S. S. 1987, *PASP*, 99, 1214
- Wenger, M., Ochsenbein, F., Egret, D., et al. 2000, *A&AS*, 143, 9
- Wright, E. L., Eisenhardt, P. R. M., Mainzer, A. K., et al. 2010, *AJ*, 140, 1868
- Wyman, M., Rudd, D. H., Vanderveld, R. A., & Hu, W. 2014, *Physical Review Letters*, 112, 051302

Table 1
Cepheids in our Sample

Name	$\log(P)$ (days)	$\langle B \rangle$ (mag)	$\langle V \rangle$ (mag)	$\langle I \rangle$ (mag)	$\langle J \rangle$ (mag)	$\langle H \rangle$ (mag)	$\langle K \rangle$ (mag)	RA ($^\circ$) (J2000)	Dec ($^\circ$) (J2000)
AQ Car	0.990	9.785	8.855	7.870	7.192	6.743	6.630	15.3457	-61.0741
AQ Pup	1.479	9.70	8.54	7.175	5.879	5.329	5.091	119.5920	-29.1301
CD Cyg	1.232	10.221	8.953	7.503	6.451	5.880	5.712	301.1107	+34.1123
DD Cas	0.992	11.111	9.880	8.580	7.552	6.952	6.908	359.3957	+62.7182
HW Car	0.964	10.122	9.125	8.027	7.258	6.704	6.596	159.8347	-61.1524
KN Cen ^a	1.531	-	9.86	-	6.27	5.92	-	204.1537	-64.5583
RY Sco ^a	1.308	-	8.19	-	-	4.3	-	267.7181	-33.7057
S Vul ^a	1.836	-	9.17	-	5.32	4.92	-	297.0992	+27.2865
SS CMa	1.092	11.136	9.925	8.470	7.434	6.849	6.677	111.5300	-25.2574
SY Aur	1.006	10.071	9.066	7.854	6.899	6.399	6.391	78.1634	+42.8318
SZ Cyg	1.179	10.909	9.430	7.797	6.573	5.886	5.746	308.2262	+46.6013
VX Per	1.037	10.459	9.307	7.995	7.076	6.517	6.292	31.9500	+58.4433
VY Car	1.277	8.616	7.455	6.279	5.463	4.944	4.804	161.1362	-57.5654
WZ Sgr	1.339	9.400	8.017	6.530	5.402	4.763	4.565	274.2488	-19.0758
X Pup	1.414	9.742	8.515	7.157	6.180	5.600	5.430	113.2072	-20.9056
XY Car	1.094	10.510	9.294	7.950	6.978	6.405	6.240	165.5669	-64.2629
XZ Car	1.221	9.861	8.604	7.251	6.313	5.745	5.585	166.0561	-60.9799
YZ Car	1.259	9.829	8.709	7.444	6.492	5.971	5.808	157.0702	-59.3502
Z Sct	1.111	10.914	9.585	8.098	7.042	6.491	6.429	280.7386	-5.8209

Note. — Cepheid data in this Table are from van Leeuwen et al. (2007), unless otherwise noted. The photometry is used for planning purposes only; our project will obtain *HST* photometry for the target Cepheids.

^a Data for this object have been obtained from the SIMBAD database (Wenger et al. 2000)

Table 2
Properties of the Reference Stars - I. UVIS Photometry

Star	<i>F275W</i> WFC3/UVIS	<i>F336W</i> WFC3/UVIS	<i>F410M</i> WFC3/UVIS	<i>F467M</i> WFC3/UVIS	<i>F547M</i> WFC3/UVIS	<i>F606W</i> WFC3/UVIS	<i>F621M</i> WFC3/UVIS	<i>F850LP</i> WFC3/UVIS
3	15.251 \pm 0.006	14.258 \pm 0.300	13.850 \pm 0.006	13.614 \pm 0.003	...
5	13.316 \pm 0.300	12.768 \pm 0.302	12.977 \pm 0.301	12.345 \pm 0.002	12.318 \pm 0.001	12.213 \pm 0.300
6	19.887 \pm 0.090	18.119 \pm 0.027	18.084 \pm 0.023	17.498 \pm 0.011	16.877 \pm 0.003	16.562 \pm 0.010	16.398 \pm 0.006	15.513 \pm 0.009
9	19.279 \pm 0.064	17.520 \pm 0.020	17.310 \pm 0.015	16.685 \pm 0.012	...	15.589 \pm 0.005	15.403 \pm 0.003	14.251 \pm 0.005
10	17.336 \pm 0.016	16.638 \pm 0.006	16.333 \pm 0.005	16.151 \pm 0.003	...
11	17.766 \pm 0.020	17.002 \pm 0.007	16.662 \pm 0.006	16.462 \pm 0.004	...
12	17.853 \pm 0.021	17.265 \pm 0.008	16.912 \pm 0.009	16.689 \pm 0.006	...
14	12.569 \pm 0.309	...	12.335 \pm 0.002	12.267 \pm 0.002	...
18	16.308 \pm 0.014	15.600 \pm 0.008	15.920 \pm 0.008	15.630 \pm 0.007	15.078 \pm 0.004	14.857 \pm 0.005	14.724 \pm 0.002	13.872 \pm 0.004
21	19.246 \pm 0.066	17.989 \pm 0.025	17.361 \pm 0.016	16.875 \pm 0.011	16.328 \pm 0.005	16.061 \pm 0.007	15.905 \pm 0.008	14.954 \pm 0.007
23	20.202 \pm 0.133	18.824 \pm 0.039	18.762 \pm 0.032	18.149 \pm 0.021	17.456 \pm 0.009	17.081 \pm 0.010	16.902 \pm 0.009	15.887 \pm 0.011
25	18.282 \pm 0.038	16.498 \pm 0.012	16.250 \pm 0.009	14.725 \pm 0.004	14.539 \pm 0.007	13.532 \pm 0.300
26	16.557 \pm 0.016	15.474 \pm 0.007	14.790 \pm 0.004	14.689 \pm 0.300	14.000 \pm 0.301	13.716 \pm 0.003	13.565 \pm 0.005	12.544 \pm 0.300
29	18.110 \pm 0.036	16.429 \pm 0.012	16.524 \pm 0.011	16.003 \pm 0.005	15.571 \pm 0.003	15.333 \pm 0.005	15.210 \pm 0.004	14.658 \pm 0.006
31	18.611 \pm 0.044	17.005 \pm 0.015	16.929 \pm 0.013	16.375 \pm 0.009	15.764 \pm 0.004	15.469 \pm 0.005	15.292 \pm 0.008	14.369 \pm 0.005
37	17.374 \pm 0.024	15.634 \pm 0.008	15.071 \pm 0.300	13.649 \pm 0.301	...	12.237 \pm 0.003	11.988 \pm 0.005	...
38	19.433 \pm 0.074	17.588 \pm 0.020	17.368 \pm 0.016	16.674 \pm 0.010	15.692 \pm 0.004	15.552 \pm 0.007	15.355 \pm 0.009	14.198 \pm 0.005
39	17.646 \pm 0.017	16.980 \pm 0.007	16.691 \pm 0.012	16.481 \pm 0.009	...
43	17.291 \pm 0.014	15.921 \pm 0.004	15.260 \pm 0.004	14.972 \pm 0.006	...
44	15.974 \pm 0.007	15.551 \pm 0.003	15.339 \pm 0.005	15.202 \pm 0.009	...
45	17.246 \pm 0.014	16.137 \pm 0.005	15.588 \pm 0.004	15.314 \pm 0.008	...
66	20.564 \pm 0.160	19.048 \pm 0.042	18.896 \pm 0.034	18.180 \pm 0.022	17.464 \pm 0.009	17.085 \pm 0.008	16.868 \pm 0.009	15.683 \pm 0.010
n1	18.424 \pm 0.028	17.785 \pm 0.011
n2	20.976 \pm 0.419	19.646 \pm 0.061	19.513 \pm 0.049	18.884 \pm 0.021	18.073 \pm 0.009	17.673 \pm 0.010	17.469 \pm 0.006	16.315 \pm 0.013
n4	23.488 \pm 1.397	20.552 \pm 0.108	20.027 \pm 0.064	18.979 \pm 0.033	17.938 \pm 0.011	17.391 \pm 0.010	17.148 \pm 0.009	15.518 \pm 0.009
n7	20.451 \pm 0.166	19.202 \pm 0.047	...	18.366 \pm 0.024	17.535 \pm 0.301	17.264 \pm 0.010	17.053 \pm 0.014	15.972 \pm 0.011
n10	23.207 \pm 1.152	20.534 \pm 0.104	19.766 \pm 0.056	18.645 \pm 0.027	17.626 \pm 0.010	17.109 \pm 0.008	16.847 \pm 0.006	15.174 \pm 0.008
n11	21.637 \pm 0.790	20.674 \pm 0.118	20.065 \pm 0.065	19.026 \pm 0.038	18.012 \pm 0.017	17.484 \pm 0.010	17.224 \pm 0.004	15.629 \pm 0.009

Note. — All *HST* photometric measurements are in the Vega system and have been obtained from data for this Project. Magnitudes in *F606W* and *F621M* are from observations obtained with spatial scanning data; other measurements are from 2×2 binned data.

Table 2
Properties of the Reference Stars - II. IR Photometry

Star	<i>J</i>	<i>F160W</i>	<i>H</i>	<i>K</i>	Channel 1	Channel 2
	2MASS	WFC3/IR	2MASS	2MASS	WISE	WISE
3	11.261 ± 0.022	...	10.642 ± 0.021	10.439 ± 0.023	10.282 ± 0.026	10.322 ± 0.026
5	11.902 ± 0.022	...	11.813 ± 0.022	11.802 ± 0.024
6	14.882 ± 0.042	...	14.375 ± 0.064	14.478 ± 0.094
9	13.575 ± 0.026	...	13.099 ± 0.021	12.996 ± 0.036
10	14.435 ± 0.027	...	13.960 ± 0.043	13.976 ± 0.058	13.880 ± 0.030	13.957 ± 0.047
11	14.573 ± 0.026	...	14.173 ± 0.035	14.014 ± 0.063	13.829 ± 0.031	14.040 ± 0.053
12	14.959 ± 0.059	...	14.374 ± 0.065	...	13.960 ± 0.032	14.049 ± 0.051
14	11.646 ± 0.024	...	11.475 ± 0.021	11.455 ± 0.024	11.358 ± 0.023	...
18	13.365 ± 0.022	...	13.162 ± 0.034	13.093 ± 0.034
21	14.342 ± 0.024	14.125 ± 0.017	14.056 ± 0.047	13.877 ± 0.059
23	...	14.840 ± 0.023
25	12.914 ± 0.024	12.581 ± 0.008	12.514 ± 0.024	12.417 ± 0.029
26	12.110 ± 0.021	11.935 ± 0.006	11.922 ± 0.024	11.761 ± 0.023
29
31	13.759 ± 0.021	13.417 ± 0.012	13.326 ± 0.022	13.282 ± 0.036
37	9.453 ± 0.022	...	8.703 ± 0.061	8.481 ± 0.019
38	13.402 ± 0.024	12.993 ± 0.010	12.876 ± 0.022	12.782 ± 0.027
39	14.910 ± 0.047	...	14.395 ± 0.044	14.219 ± 0.073
43	11.741 ± 0.030	...	10.762 ± 0.028	10.492 ± 0.024	...	10.336 ± 0.022
44	...	14.449 ± 0.015
45	12.555 ± 0.022	...	11.749 ± 0.026	11.486 ± 0.021	...	11.406 ± 0.023
66	...	14.484 ± 0.020
n1	15.631 ± 0.062	...	15.543 ± 0.118	15.515 ± 0.216	15.014 ± 0.042	...
n2	15.663 ± 0.055	...	15.020 ± 0.059
n4	14.480 ± 0.036	13.879 ± 0.015	13.704 ± 0.026	13.475 ± 0.035
n7	15.319 ± 0.037	14.901 ± 0.024	14.802 ± 0.047
n10	14.145 ± 0.035	...	13.400 ± 0.029	13.119 ± 0.033
n11	14.671 ± 0.027	...	13.888 ± 0.038	13.780 ± 0.046

Note. — All *HST* photometric measurements are in the Vega system and have been obtained from data for this Project. Photometry obtained from the 2MASS Survey (Skrutskie et al. 2006) and from *WISE* (Wright et al. 2010) are in their respective systems.

Table 2
Properties of the Reference Stars - III. Spectra, Classification, and Astrometry

Star	RA (° (J2000))	Dec (° (J2000))	Spectrum Source	Class ^a	Quality ^b	T_{eff}^c (K)	π_{full}^d (mas)	π_{astro}^e (mas)
3	111.49716	-25.23251	Gemini	K0 IV	F	5340 ± 160	0.414 ± 0.043	0.166 ± 0.110
5	111.51980	-25.24066	Gemini	A7 V	G	7920 ± 250	1.185 ± 0.049	1.197 ± 0.053
6	111.51377	-25.26266	Gemini	G5 IV	VG	5730 ± 110	0.746 ± 0.045	0.758 ± 0.051
9	111.53022	-25.23712	Lick	G0 IV–V	VG	6180 ± 180
10	111.54177	-25.23063	Gemini	F7 IV	VG	6550 ± 200	0.448 ± 0.096	0.060 ± 0.260
11	111.52409	-25.22336	Lick	F8 III	F	6420 ± 160
12	111.51990	-25.22623	Gemini	K5 IV	VG	4600 ± 260
14	111.51993	-25.23608	Lick	F5 IV–V	VG	6700 ± 130	1.747 ± 0.061	1.766 ± 0.063
18	111.51415	-25.25188	Lick	B2 V	F	21000 ± 1000	0.281 ± 0.023	0.339 ± 0.041
21	111.53000	-25.26841	Gemini	A4 III–IV	VG	8400 ± 340	0.333 ± 0.027	0.297 ± 0.036
23	111.53011	-25.26374	Gemini	F8 V	VG	6420 ± 160	0.398 ± 0.036	0.386 ± 0.040
25	111.54306	-25.27473	Lick	G5 IV–V	G	5730 ± 110	0.688 ± 0.037	0.683 ± 0.040
26	111.52272	-25.28065	Lick	A2 III–IV	VG	8680 ± 360
29	111.53344	-25.25502	Gemini	G6 V	VG	5690 ± 130	1.012 ± 0.038	1.023 ± 0.041
31	111.54654	-25.27182	Gemini	F8 IV	VG	6420 ± 160	0.636 ± 0.038	0.644 ± 0.042
37	111.54825	-25.26604	Gemini	G2 III	VG	5620 ± 180
38	111.53878	-25.26636	Lick	G0 V	VG	6180 ± 180	0.661 ± 0.031	0.699 ± 0.035
39	111.56396	-25.28153	Lick	G0 V	F	5920 ± 180	0.730 ± 0.092	0.789 ± 0.117
43	111.52175	-25.28641	Keck	K6 Iab	G	5500 ± 260	0.032 ± 0.008	0.018 ± 0.064
44	111.52294	-25.28780	Lick	G2 IV–V	G	5800 ± 180	0.797 ± 0.037	0.799 ± 0.039
45	111.53057	-25.28724	Lick	F8 II–III	F	6300 ± 130	0.257 ± 0.022	0.336 ± 0.053
66	111.55038	-25.26568	Lick	G2 III	G	5620 ± 180	0.366 ± 0.040	0.337 ± 0.071
n1	111.50797	-25.23456	Lick	B9 ^f	P	...	0.548 ± 0.063	0.548 ± 0.074
n2	111.51711	-25.26131	Keck	F7 III–IV	G	6480 ± 200
n4	111.52766	-25.26668	Keck	G5 ^f	F	5660 ± 110	0.240 ± 0.024	0.124 ± 0.043
n7	111.54059	-25.26129	Keck	F7 V	G	6480 ± 200
n10	111.55420	-25.25736	Keck	G5 ^f	G	5660 ± 110
n11	111.50804	-25.25449	Keck	G9 IV–V	G	5390 ± 160	0.331 ± 0.036	0.376 ± 0.060

^a Spectral classification based on MKCLASS Version 1.7 (Gray & Corbally 2014) (see text for details) unless otherwise noted

^b Classification quality from MKCLASS; VG=Very good, G=Good, F=Fair, P=Poor

^c Temperature and uncertainty from the spectroscopic analysis

^d Parallax estimate based on combined spectrophotometric and astrometric data

^e Parallax estimate based purely on astrometric data for each star; spectrophotometric information is retained for all other stars. See Section 4.2 for details.

^f Classification and quality from match to model spectra; luminosity class not available

Table 3
Spatial Scanning Observations Used in this Paper

Date	Rootname	Program ID	EXPSTART (MJD)	Filter	Exp. time (seconds)	Scan rate ($''\text{s}^{-1}$)	Scan length ($''$)	Number of legs	X pos targ ($''$)
Observations for SS CMa									
2012-10-23	ibzc04kjq	12879	56223.905323	<i>F606W</i>	350.0	0.330	115.5	1	-3.00
2012-10-23	ibzc04klq	12879	56223.911133	<i>F621M</i>	350.0	0.330	115.5	1	-3.00
2012-10-23	ibzc04knq	12879	56223.916712	<i>F621M</i>	350.0	0.330	115.5	1	-3.00
2012-10-23	ibzc04kpq	12879	56223.922592	<i>F606W</i>	350.0	0.330	115.5	1	-3.00
2012-10-23	ibzc04krq	12879	56223.928899	<i>F606W</i>	350.0	1.505	526.7	3	-10.00
2013-04-18	ibzc15ntq	12879	56400.332005	<i>F606W</i>	348.0	0.330	114.8	1	-3.00
2013-04-18	ibzc15nvq	12879	56400.337792	<i>F621M</i>	348.0	0.330	114.8	1	-3.00
2013-04-18	ibzc15nxq	12879	56400.343347	<i>F621M</i>	348.0	0.330	114.8	1	-3.00
2013-04-18	ibzc15o0q	12879	56400.349204	<i>F606W</i>	348.0	0.330	114.8	1	-3.00
2013-04-18	ibzc15o2q	12879	56400.355489	<i>F606W</i>	348.0	1.505	523.7	3	-10.00
2013-10-22	ic8z04haq	13344	56587.580458	<i>F606W</i>	348.0	0.330	114.8	1	-3.00
2013-10-22	ic8z04hcq	13344	56587.586246	<i>F621M</i>	348.0	0.330	114.8	1	-3.00
2013-10-22	ic8z04heq	13344	56587.591801	<i>F621M</i>	348.0	0.330	114.8	1	-3.00
2013-10-22	ic8z04hgq	13344	56587.597657	<i>F606W</i>	348.0	0.330	114.8	1	-3.00
2013-10-22	ic8z04hiq	13344	56587.603942	<i>F606W</i>	348.0	1.505	523.7	3	-10.00
2014-04-16	ic8z15o4q	13344	56763.310662	<i>F606W</i>	348.0	0.330	114.8	1	+3.00
2014-04-16	ic8z15o6q	13344	56763.316449	<i>F621M</i>	348.0	0.330	114.8	1	+3.00
2014-04-16	ic8z15o8q	13344	56763.322005	<i>F621M</i>	348.0	0.330	114.8	1	+3.00
2014-04-16	ic8z15oaaq	13344	56763.327862	<i>F606W</i>	348.0	0.330	114.8	1	+3.00
2014-04-16	ic8z15oocq	13344	56763.334146	<i>F606W</i>	348.0	1.505	523.7	3	+2.00
2014-10-23	icir03ixq	13678	56953.729151	<i>F606W</i>	348.0	0.330	114.8	1	-3.00
2014-10-23	icir03j3q	13678	56953.746350	<i>F606W</i>	348.0	0.330	114.8	1	-3.00
2014-10-23	icir03izq	13678	56953.734938	<i>F621M</i>	348.0	0.330	114.8	1	-3.00
2014-10-23	icir03j1q	13678	56953.740494	<i>F621M</i>	348.0	0.330	114.8	1	-3.00
Observations for M48									
2014-09-25	icmp04ptq	13929	56925.069671	<i>F673N</i>	348.0	0.400	139.2	1	-6.90
2014-09-25	icmp04pvq	13929	56925.075678	<i>F673N</i>	348.0	0.400	139.2	1	-33.10
2014-09-25	icmp04pyq	13929	56925.081812	<i>F673N</i>	348.0	0.400	139.2	1	+26.20
2014-09-25	icmp04q0q	13929	56925.087738	<i>F673N</i>	348.0	0.400	139.2	1	+14.40
2014-09-25	icmp04q2q	13929	56925.131662	<i>F673N</i>	348.0	0.400	139.2	1	+43.50
2014-09-25	icmp06qnq	13929	56925.274092	<i>F673N</i>	348.0	0.400	139.2	1	+8.50
2014-09-25	icmp06qpq	13929	56925.280227	<i>F673N</i>	348.0	0.400	139.2	1	+57.50
2014-09-25	icmp06qrr	13929	56925.286199	<i>F673N</i>	348.0	0.400	139.2	1	-12.00
2014-09-25	icmp06qtq	13929	56925.337796	<i>F673N</i>	348.0	0.400	139.2	1	+17.40
2014-09-25	icmp06qvq	13929	56925.343907	<i>F673N</i>	348.0	0.400	139.2	1	-24.00
2014-09-28	icmp05xlq	13929	56928.863641	<i>F673N</i>	348.0	0.400	139.2	1	-21.20
2014-09-28	icmp05xnnq	13929	56928.869741	<i>F673N</i>	348.0	0.400	139.2	1	+36.30
2014-09-28	icmp05xprq	13929	56928.907391	<i>F673N</i>	348.0	0.400	139.2	1	+16.30
2014-09-28	icmp05xrq	13929	56928.913410	<i>F673N</i>	348.0	0.400	139.2	1	-47.20
2014-09-28	icmp05xtq	13929	56928.919486	<i>F673N</i>	348.0	0.400	139.2	1	+3.30
2014-09-29	icmp01gmq	13929	56929.974255	<i>F621M</i>	348.0	0.400	139.2	1	-6.90
2014-09-29	icmp01goq	13929	56929.980261	<i>F621M</i>	348.0	0.400	139.2	1	-33.10
2014-09-29	icmp01gqq	13929	56929.986396	<i>F621M</i>	348.0	0.400	139.2	1	+26.20
2014-09-29	icmp01gsq	13929	56929.992322	<i>F621M</i>	348.0	0.400	139.2	1	+14.40
2014-09-29	icmp01guq	13929	56929.998340	<i>F621M</i>	348.0	0.400	139.2	1	+43.50
2014-09-30	icmp03h5q	13929	56930.039567	<i>F621M</i>	348.0	0.400	139.2	1	+8.50
2014-09-30	icmp03haq	13929	56930.045701	<i>F621M</i>	348.0	0.400	139.2	1	+57.50
2014-09-30	icmp03hcq	13929	56930.051674	<i>F621M</i>	348.0	0.400	139.2	1	-12.00
2014-09-30	icmp03hfq	13929	56930.057819	<i>F621M</i>	348.0	0.400	139.2	1	+17.40
2014-09-30	icmp03hhq	13929	56930.063931	<i>F621M</i>	348.0	0.400	139.2	1	-24.00
2014-10-01	icmp02odq	13929	56931.174394	<i>F621M</i>	348.0	0.400	139.2	1	-21.20
2014-10-01	icmp02ofq	13929	56931.180493	<i>F621M</i>	348.0	0.400	139.2	1	+36.30
2014-10-01	icmp02ohq	13929	56931.186662	<i>F621M</i>	348.0	0.400	139.2	1	+16.30
2014-10-01	icmp02ojq	13929	56931.192681	<i>F621M</i>	348.0	0.400	139.2	1	-47.20
2014-10-01	icmp02opq	13929	56931.236743	<i>F621M</i>	348.0	0.400	139.2	1	+3.30

Table 3
Spatial Scanning Observations Used in this Paper (continued)

Date	Rootname	Program ID	EXPSTART (MJD)	Filter	Exp. time (seconds)	Scan rate ($''\text{ s}^{-1}$)	Scan length ($''$)	Number of legs	X pos targ ($''$)
Observations for M67									
2014-11-08	icmp07m8q	13929	56969.071721	<i>F606W</i>	348.0	0.400	139.2	1	-30.34
2014-11-08	icmp07maq	13929	56969.077670	<i>F606W</i>	348.0	0.400	139.2	1	-14.35
2014-11-08	icmp07mdq	13929	56969.083758	<i>F606W</i>	348.0	0.400	139.2	1	+30.88
2014-11-08	icmp07mfq	13929	56969.132601	<i>F606W</i>	348.0	0.400	139.2	1	+36.42
2014-11-08	icmp07mhq	13929	56969.138955	<i>F606W</i>	348.0	0.400	139.2	1	+39.60
2014-11-08	icmp08nyq	13929	56969.524129	<i>F606W</i>	350.0	0.400	140.0	1	+7.05
2014-11-08	icmp08o0q	13929	56969.530055	<i>F606W</i>	350.0	0.400	140.0	1	-2.88
2014-11-08	icmp08o2q	13929	56969.536003	<i>F606W</i>	350.0	0.400	140.0	1	+8.96
2014-11-08	icmp08o4s	13929	56969.541988	<i>F606W</i>	350.0	0.400	140.0	1	+26.71
2014-11-08	icmp08o6s	13929	56969.547902	<i>F606W</i>	350.0	0.400	140.0	1	+18.54
2014-11-08	icmp10q6q	13929	56969.922312	<i>F606W</i>	350.0	0.400	140.0	1	+3.90
2014-11-08	icmp10q8q	13929	56969.928295	<i>F606W</i>	350.0	0.400	140.0	1	+0.28
2014-11-08	icmp10qaq	13929	56969.934302	<i>F606W</i>	350.0	0.400	140.0	1	+3.89
2014-11-08	icmp10qcq	13929	56969.940321	<i>F606W</i>	350.0	0.400	140.0	1	-16.75
2014-11-08	icmp10qeq	13929	56969.946281	<i>F606W</i>	350.0	0.400	140.0	1	-22.13
2014-11-09	icmp09vkq	13929	56970.851154	<i>F606W</i>	350.0	0.400	140.0	1	-5.14
2014-11-09	icmp09vmq	13929	56970.857022	<i>F606W</i>	350.0	0.400	140.0	1	+13.52
2014-11-09	icmp09voq	13929	56970.862890	<i>F606W</i>	350.0	0.400	140.0	1	-8.37
2014-11-09	icmp09vqq	13929	56970.868886	<i>F606W</i>	350.0	0.400	140.0	1	+15.69
2014-11-09	icmp09vsq	13929	56970.874777	<i>F606W</i>	350.0	0.400	140.0	1	+2.15